

REPORT DOCUMENTATION PAGE			Form Approved OMB No. 0704-0188
<small>Public reporting burden for this collection of information is estimated to average 1 hour per response, including the time for reviewing instructions, searching existing data sources, gathering and maintaining the data needed, and completing and reviewing the collection of information. Send comments regarding this burden estimate or any other aspect of this collection of information, including suggestions for reducing this burden, to Washington Headquarters Services, Directorate for Information Operations and Reports, 1215 Jefferson Davis Highway, Suite 1204, Arlington, VA 22202-4302, and to the Office of Management and Budget, Paperwork Reduction Project (0704-0188), Washington, DC 20503.</small>			
1. AGENCY USE ONLY (Leave blank)	2. REPORT DATE 17 Apr 97	3. REPORT TYPE AND DATES COVERED	
4. TITLE AND SUBTITLE A MICROMECHANICAL SILICON OSCILLATING ACCELEROMETER		5. FUNDING NUMBERS	
6. AUTHOR(S) KEVIN A. GIBBONS			
7. PERFORMING ORGANIZATION NAME(S) AND ADDRESS(ES) MASSACHUSETTS INSTITUTE OF TECHNOLOGY, CAMBRIDGE MA		8. PERFORMING ORGANIZATION REPORT NUMBER 97-016	
9. SPONSORING/MONITORING AGENCY NAME(S) AND ADDRESS(ES) DEPARTMENT OF THE AIR FORCE AFIT/CI 2950 P STRRET WRIGHT-PATTERSON AFB OH 45433-7765		10. SPONSORING/MONITORING AGENCY REPORT NUMBER	
11. SUPPLEMENTARY NOTES			
12a. DISTRIBUTION AVAILABILITY STATEMENT <div style="border: 1px solid black; padding: 5px; width: fit-content; margin: 10px auto;"> DISTRIBUTION STATEMENT A Approved for public release; Distribution Unlimited </div>		12b. DISTRIBUTION CODE	
13. ABSTRACT (Maximum 200 words)			
14. SUBJECT TERMS		15. NUMBER OF PAGES 102	
		16. PRICE CODE	
17. SECURITY CLASSIFICATION OF REPORT	18. SECURITY CLASSIFICATION OF THIS PAGE	19. SECURITY CLASSIFICATION OF ABSTRACT	20. LIMITATION OF ABSTRACT

19970424 027

A MICROMECHANICAL SILICON OSCILLATING ACCELEROMETER

by

KEVIN A. GIBBONS

B.S. Mechanical Engineering
The Pennsylvania State University
(1992)

SUBMITTED TO THE DEPARTMENT OF MECHANICAL ENGINEERING
IN PARTIAL FULFILLMENT OF THE REQUIREMENTS
FOR THE DEGREE OF

MASTER OF SCIENCE IN MECHANICAL ENGINEERING

at the

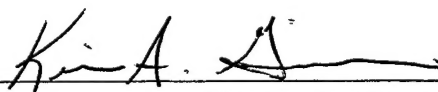
MASSACHUSETTS INSTITUTE OF TECHNOLOGY

February 1997

© Kevin A. Gibbons, 1997. All rights reserved.

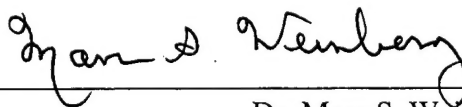
The author hereby grants to M.I.T. and The Charles Stark Draper Laboratory, Inc.
permission to reproduce and distribute copies of the thesis in whole or in part.

Signature of Author_____



Department of Mechanical Engineering

Approved by_____



Dr. Marc S. Weinberg

Technical Supervisor, Draper Laboratory

Certified by_____



Dr. David L. Trumper

Thesis Advisor

Accepted by_____



Dr. Ain A. Sonin

Chairman, Departmental Committee of Graduate Students

ACKNOWLEDGMENTS

I would like to thank several folks for their assistance in completing my thesis work at Draper Laboratory while attending MIT.

I am grateful to my technical advisors, Dr. Marc S. Weinberg and Dr. David L. Trumper, along with Dr. David S. Nokes, for their expert assistance. With their guidance, I have been able to accomplish my research goals.

The Draper Laboratory's microfabrication team has been an inspiration. Jeff Borenstein, James Campbell, Connie Cardoso, Jimmy 'SOA' Cousens, Bobby Fields, Brenda Hugh, Michele Lind, Susan McNeil, Lance Niles, Doug Preble and others are the team that know what they are doing and enjoy teaching others about their technical expertise. This team's generosity, kindness, and friendship shall never be forgotten.

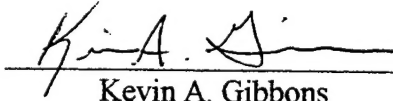
Thanks to Jamie Bolotin, Rob Bousquet, Ed Foster, Tony Kourepenis, and Tony Petrovich for their efforts in packaging, electronics, and testing. Without their dedication there would be no test data to report.

Thank you, Janet and Harry Gibbons, for instilling in me a desire to do my best, and to always complete what I have started. Mom and Dad, I pray to God that I am able to encourage my family with love, the way you have and continue to encourage me.

My wife has been my greatest inspiration and my best friend especially through the challenging times. Thank you, Barbara Ann, for your assistance and patience during our MIT and Boston experiences. I look forward to the many great life experiences that lie ahead for us together. I am thankful and honored to be forever yours.

This thesis was prepared at the Charles Stark Draper Laboratory, Inc., under IR&D project number 15868. Publication of this thesis does not constitute approval by Draper or the sponsoring agency of the findings or conclusions contained herein. It is published for the exchange and stimulation of ideas.

I hereby assign my copyright of this thesis to The Charles Stark Draper Laboratory, Inc., Cambridge Massachusetts.



Kevin A. Gibbons
January 28, 1997

Permission is hereby granted by The Charles Stark Draper Laboratory, Inc., to the Massachusetts Institute of Technology to reproduce any or all of this thesis.

A MICROMECHANICAL SILICON OSCILLATING ACCELEROMETER

by

KEVIN A. GIBBONS

Submitted to the Department of Mechanical Engineering
of the Massachusetts Institute of Technology
on February 6, 1997 in partial fulfillment of the
requirements for the Degree of Master of Science in
Mechanical Engineering

ABSTRACT

This thesis describes the design and testing of a silicon oscillating accelerometer (SOA). The SOA is a silicon, micromechanical, oscillating beam accelerometer. The accelerometer is configured with two silicon tuning fork oscillators that are electrostatically driven and sensed in their out-of-phase vibrational resonance. The oscillators move on flexure beams which are configured to have one end anchored and the other end fixed to a shared seismic mass. When the seismic mass experiences an input acceleration, one oscillator's vibrating beams are loaded in tension while the other oscillator's beams are loaded in compression. This loading causes an increase and decrease in the respective oscillator's natural frequency. This change in frequency is proportional to the input acceleration. Automatic gain control electronics regulate the oscillation amplitude at resonance. The two oscillator's frequency outputs are differenced to exploit common mode error rejection.

The SOA has been fabricated from single crystal silicon using a bulk-dissolved-wafer on glass micromachining process. It is vacuum-packaged in a leadless ceramic chip carrier to achieve high quality factor and thus a sharp resonance.

Results of both closed-form and finite-element analyses are described and are in good agreement. Sensors were fabricated and experimental data including quality factor, input acceleration sensitivity or scale factor, and oscillator temperature sensitivity results are presented. An oscillator frequency of 27 kHz, a Q factor over 100,000, a scale factor of 4 Hz per g, and an oscillator temperature sensitivity of 0.4 Hz per degree Celsius have been achieved. The experimental data is shown to be in agreement with analysis results.

Thesis Supervisor: David L. Trumper
Rockwell Associate Professor
Department of Mechanical Engineering
Massachusetts Institute of Technology

CONTENTS

	<u>Page</u>
ACKNOWLEDGMENTS	2
ABSTRACT	3
CONTENTS	4
LIST OF FIGURES	6
LIST OF TABLES	10
1.0 INTRODUCTION	11
1.1 Overview of objective, design analysis, and results	11
1.2 Micromechanical devices	13
1.3 Silicon Oscillating Accelerometer (SOA) description	17
2.0 BACKGROUND	22
2.1 Theory of operation	22
2.2 The microfabrication process	36
3.0 DESIGN ANALYSIS	39
3.1 Preliminary mechanical design calculations	39
3.2 Detailed mechanical design	46
4.0 EXPERIMENTAL PROCEDURE	66
4.1 Microfabrication of the SOA	66
4.2 Preliminary testing	69
4.3 Packaging and electronics	76
4.4 SOA testing and results	78

5.0 CONCLUSIONS AND RECOMMENDATIONS	87
REFERENCES	90
LIST OF APPENDICES	92
Appendix A: Preliminary Design Spreadsheet	93
Appendix B Corning #7740 Pyrex Material Information Sheet	96
Appendix C: Preliminary Design Spreadsheet Data	100

LIST OF FIGURES

	<u>Page</u>
Figure 1.1: Draper Laboratory's Pendulous Mass Accelerometer	17
Figure 1.2: Silicon Oscillating Accelerometer (SOA) Schematic	20
Figure 2.1: Model of a Single SOA Oscillator Mass and Flexures	23
Figure 2.2: Oscillator Mass and Flexures Modeled as Lumped Parameters	26
Figure 2.3: Free Body Diagrams of SOA Components Showing Load Distribution	26
Figure 2.4: Two Engaged Electrostatic Comb Teeth	27
Figure 2.5: Model of Preamplifier Electronics and Sense Capacitance	31
Figure 2.6: Silicon-On-Glass Bulk Dissolved-Wafer Process	36
Figure 3.1: Simplified SOA Schematic	39
Figure 3.2: Preliminary Design Natural Frequency versus Beam Width	42
Figure 3.3: Preliminary Design Natural Frequency versus Oscillating Mass Width	43
Figure 3.4: Preliminary Design Scale Factor versus Beam Width	43
Figure 3.5: Preliminary Design Scale Factor versus Oscillating Mass Width	44
Figure 3.6: Preliminary Design Scale Factor versus Seismic Mass Width, α	44
Figure 3.7: Quarter SOA Finite Element Model	47
Figure 3.8: Deformed SOA Quarter Model Showing In-Phase or Out-of-Phase Mode Shapes	49
Figure 3.9: SOA FEA Natural Frequencies versus Flexure Width	54

Figure 3.10:	SOA FEA Scale Factor versus Flexure Width	55
Figure 3.11:	SOA FEA Temperature Sensitivity versus Flexure Width	55
Figure 3.12:	SOA Full Finite Element Model	56
Figure 3.13:	In-Plane Out-of-Phase Vibrational Mode Displacement Plot	57
Figure 3.14a:	SOA Out-of-Plane Vibrational Mode shown as normalized displacement contours; 10.4 kHz	59
Figure 3.14b:	SOA Out-of-Plane Vibrational Mode shown as normalized displacement contours; 10.6 kHz	59
Figure 3.14c:	SOA Out-of-Plane Vibrational Mode shown as normalized displacement contours; 12.3 kHz	59
Figure 3.14d:	SOA Out-of-Plane Vibrational Mode shown as normalized displacement contours; 13.3 kHz	59
Figure 3.14e:	SOA Out-of-Plane Vibrational Mode shown as normalized displacement contours; 20.8 kHz	60
Figure 3.14f:	SOA Out-of-Plane Vibrational Mode shown as normalized displacement contours; 28.6 kHz	60
Figure 3.14g:	SOA Out-of-Plane Vibrational Mode shown as normalized displacement contours; 30.2 kHz	60
Figure 3.14h:	SOA Out-of-Plane Vibrational Mode shown as normalized displacement contours; 32.3 kHz	60
Figure 3.15:	Half SOA Oscillator Finite Element Model	61
Figure 3.16:	Oscillator Nonlinear Stiffness Characteristic	62
Figure 3.17a:	Square Plate Supported at Four Points	64
Figure 3.17b:	Square Plate Supported at Center Point	64
Figure 4.1:	Microfabricated SOA Chip on a Penny to Show Scale	66
Figure 4.2:	Top View Photomicrograph of the SOA	67

Figure 4.3:	SEM of SOA 12 Micron Thick Oscillator Mass and Flexure	68
Figure 4.4:	SEM of SOA 12 Micron Thick Electrostatic Comb Teeth	68
Figure 4.5:	Probe Test Electrical Excitation Model	69
Figure 4.6:	SOA Oscillator In-Phase Vibrational Mode Excitation and Resulting Deformed Mode Shape at Probe Test	72
Figure 4.7:	SOA Oscillator Out-of-Phase Vibrational Mode Excitation and Resulting Deformed Mode Shape at Probe Test	73
Figure 4.8:	Analytical and Experimental SOA Out-of-Phase Oscillation Resonant Frequency Versus Flexure Width	75
Figure 4.9:	Analytical and Experimental SOA In-Phase Oscillation Resonant Frequency Versus Flexure Width	75
Figure 4.10:	SOA Brazed into LCCC with Wirebonds	76
Figure 4.11:	SOA LCCC Mounted on Preamplifier Substrate	77
Figure 4.12:	SOA Oscillator Resonance Peak In Vacuum	78
Figure 4.13a:	SOA ± 1 g Inversion Test Top Oscillator Frequency Response	80
Figure 4.13b:	SOA ± 1 g Inversion Test Bottom Oscillator Frequency Response	80
Figure 4.13c:	SOA ± 1 g Inversion Test Total Instrument Response	81
Figure 4.14a:	SOA ± 1 g Inversion Test Top Oscillator Frequency Response	81
Figure 4.14b:	SOA ± 1 g Inversion Test Bottom Oscillator Frequency Response	82
Figure 4.14c:	SOA ± 1 g Inversion Test Total Instrument Response	82
Figure 4.15:	Analytical and Experimental SOA Scale Factor versus Flexure Width	83
Figure 4.16a:	SOA Oscillator Temperature Response	85

Figure 4.16b: SOA Oscillator Temperature Response	85
Figure 5.1: Improved Probe Test Electrical Configuration	89

LIST OF TABLES

	<u>Page</u>
Table 3.1: Estimated Electrostatic Drive and Sense Parameters	45
Table 3.2: FEA Modal Results for Three Flexure Widths and Three Base Beam Widths	52
Table 3.3: SOA Maximum Displacement for 100 g Loading in the Primary Directions	63
Table 3.4: Square Plate Natural Frequencies for Four Supports and One Center Support	65
Table 4.1: SOA Probe Test Results for Out-of-Phase and In-Phase Oscillation Frequency	74

1.0 INTRODUCTION

1.1 Overview of objective, design analysis, and results

The objective of this research is to design, fabricate, and evaluate a silicon oscillating accelerometer. This accelerometer is microfabricated with the active area having dimensions of 3,400 microns by 3,400 microns. The accelerometer works on the principle that under acceleration a seismic mass applies forces to flexure beams of two oscillators. These forces shift the oscillation frequencies of the oscillators. The differential frequency shift is a measure of the sensor acceleration.

My main contribution is the design and analysis work presented in section 3.0 of this thesis. Novel design features that I developed during this work include positioning the accelerometer mass anchors, as well as the two oscillators, inside the perimeter of the silicon structure. These features enabled me to place out-of-plane modes at least ten percent away from the primary operation frequency, as described in section 3.2. They also allowed for more complete usage of the available surface area on the glass substrate. I contributed heavily in the CAD layout, microfabrication, packaging, and device testing, although the majority of the implementation effort in each of these areas was performed by Draper Laboratory engineers and technicians specialized in those areas.

I am providing an overview of design analysis and test results in this section. A more detailed description of this data is located in this thesis in the sections listed. I performed the design analysis in two phases; a closed-form spreadsheet analysis and a detailed finite element analysis.

The closed-form solution, performed first and described in section 3.1, provided insight into the critical physical effects and their relationship to physical parameters

which I could vary in the design. Through this analysis, I obtained an estimate of the operating frequency, device sensitivity, and electrostatic force and sense parameters. Figures 3.2 through 3.6 and table 3.2 show these results. I estimated operating frequency to be twenty five kilohertz and the instrument sensitivity to be 3.9 hertz per g. I also estimated that with reasonable excitation parameter values, as in table 3.1, an acceptable sensor output signal amplitude of 0.005 volts peak could be achieved. These results showed the feasibility of the SOA and thus the effort of detailed design was merited. These estimates also served as an independent check for consistency of the finite element results in section 3.2.

I developed three finite element models for the detailed design effort; a quarter SOA model, a full SOA model, and a half oscillator model. The description of these analyses is given in section 3.2.

Using the quarter model and an in-plane element formulation, I calculated the out-of-phase oscillator frequency to be 25.1 kHz, the in-phase oscillator frequency to be 21.6 kHz, the instrument sensitivity to input acceleration to be 4.0 Hz/g, and the thermal effect of the glass base of the SOA stretching the silicon structure to be 1.03 Hz/°C.

I calculated out-of-plane instrument resonant frequencies using the full SOA model and an out-of-plane element formulation. This analysis showed that no other mode frequencies were within ten percent of the desired operational resonant frequency of the oscillators, an important feature in order to allow reliable amplitude stabilization of the operating mode.

Bias stability due to oscillator stiffness nonlinearity was estimated to be 30 microg's by determining the stiffness nonlinearity characteristic through a nonlinear

analysis using the half oscillator finite element model. The bias stability due to thermal effects was also calculated to be 100 microg's; due to a calculated oscillator frequency shift of 0.4 Hz/°C.

These accelerometers were fabricated and tested as described in sections 4.1 through 4.4. Probe test results, given in table 4.1, showed an out-of-phase operating frequency of 28 kHz and an in-phase frequency of 24 kHz. Scanning electron micrographs showed flexure widths of 0.3 microns wider than designed. Sealed units showed quality factors on the order of 100,000. A scale factor of 3.5 Hz/g and an oscillator temperature sensitivity of 0.4 Hz/°C were measured experimentally. Anomalies in the test results are discussed and recommendations for future work are presented in section 5.0.

1.2 Micromechanical devices

Many applications exist for micromechanical devices and sensors. These applications include use in: automobile safety systems such as airbag deployment and anti-lock brake controllers; shock sensing alarms; natural phenomena measurement apparatus; automated assembly and robotic control systems; and inertial systems. The microelectromechanical systems worldwide market has been projected in the Batelle Frankfurt Micromechanics Study [1] to grow from approximately seven hundred million dollars in 1990 to approximately twelve billion dollars by the year 2000. This growth is fueled by the many advantages and applications that micromechanical devices have already demonstrated.

The advantages of the micromechanical instrument family are their small size and weight coupled with performance. Micromechanical instruments are also seen as a possible solution to the problem of high cost of fabrication and maintenance of currently used instruments, especially inertial instruments. Similar to the photolithographic processes used in integrated circuit manufacturing, micromechanical fabrication techniques could produce hundreds of viable units on one silicon wafer in the order of days by a highly automated manufacturing process. Control, readout and self-test electronics have already been fabricated and demonstrated on the same chip as the sensing unit. These features would give rise to the same large-quantity and low-cost manufacturing found in the integrated circuit industry [2]. Maintenance of these micromechanical units could be reduced to replacing defective or aged components with new sensors in integrated circuit chips, instead of the time consuming and costly disassembly, individual part replacement or cleaning, and reassembly of conventional units. A typical conventional electro-mechanical accelerometer can be composed of hundreds of precisely machined, aligned, and assembled components. These conventional instruments consist of a complex arrangement of precision bearings, floats, gimbals, and offset center of gravity masses. Such precision instruments are expensive to manufacture and maintain. Micromechanical sensors, through bulk manufacturing technology, have the potential of greatly reducing initial and life cycle costs of instrument systems. One class of instruments, the inertial measurement unit, is a prime target area to study for this reduction of initial and life cycle costs of micromechanical systems. Accelerometers have been a focus of this development since the 1970's [3].

Micromechanical accelerometers have been designed and fabricated from such materials as quartz and silicon employing solid state manufacturing techniques [4]. Silicon devices have been produced from single crystal silicon, polycrystalline silicon, as well as composites including silicon [5],[6].

Draper Laboratory has opted to design and fabricate its micromechanical devices, including micromechanical accelerometers, from single crystal silicon (SCS). An advantage of this SCS selection is the mechanical properties being close to theoretical values, so that minimal hysteresis and creep are exhibited [7]. Another advantage is that high purity SCS is readily available because of its widespread use by the semiconductor industry. Many issues, such as material thermal response mismatch and bond integrity, are eliminated because no plating or post process bonding of mass to the silicon structure is necessary. The flexibility of the microfabrication process used by Draper Laboratory accommodates relatively thick builds so that complete, single crystal silicon structures are feasible. The changing Young's modulus of silicon with temperature and the thermal expansion coefficient mismatch between silicon and the Pyrex base enable the design of thermally insensitive oscillators, as described in section 3.1; a feature not afforded by quartz.

The boundary conditions produced by the electrostatic bonding of the silicon structure to the glass have proven to be very effective by producing high Q factor, or quality factor, oscillators. Low Q factor can indicate interactions between the structure and its base at the boundary or bond site; often hysteresis, which degrades performance. The bond sites of the silicon to the base in Draper Laboratory's microfabrication process are small compared to the glass base and distant from the glass attachment to the chip

carrier both contributing to high Q factor. High Q factor is important in achieving a sharp oscillator resonance so that the natural frequency of fabricated silicon oscillators can be properly measured and the amplitude of oscillation can be precisely controlled.

Draper Laboratory has used single crystal silicon in the fabrication of several micromechanical instruments including a tuning fork gyroscope and a force rebalance accelerometer [8]. Draper Laboratory has been studying micromechanical accelerometers for eight years. Most of the work has been focused on a pendulous mass accelerometer design, shown in figure 1.1, that can be operated in either an open loop or closed loop force rebalanced configuration [8].

The sensitivity and stability of these micromechanical instruments are the characteristics that determine their usefulness in inertial systems. There exist several specifications that micromechanical accelerometers are required to match or exceed, besides being small, reliable, lightweight, and low-cost, to make them acceptable replacements for current high performance accelerometers. These specifications include: micro-g stability, able to measure accurately in the region of ten g's of acceleration, and viability up to one hundred g's acceleration. Vibration disturbance rejection up to two kilohertz (kHz) would be required as well as radiation hardness, and the ability to continue operation through an interruption of electronics output. Draper Laboratory's study of micromechanical tuning fork gyroscopes [8] and a quartz resonator accelerometer and desire for even greater reliability than the micromechanical force-rebalanced accelerometers have led to the Silicon Oscillating Accelerometer (SOA) program. The SOA is being studied to evaluate the concept's potential of eventually

becoming a replacement for current inertial system units. Several design, build, and test iterations will be required before ultimate specifications can be met. This first SOA design will be used to evaluate both modeling and microfabrication capabilities in order to demonstrate the potential of this technology for inertial applications.

1.3 The Silicon Oscillating Accelerometer (SOA) description

The Silicon Oscillating Accelerometer, or SOA, design described in this thesis is shown as a schematic in figure 1.2. The single crystal silicon structure is mounted on Corning #7740 Pyrex glass, via nine bond sites. Two large cutouts in the silicon contain the oscillators which are driven electrostatically at resonance. These resonators are joined via ligaments to the remainder of the silicon which forms the seismic

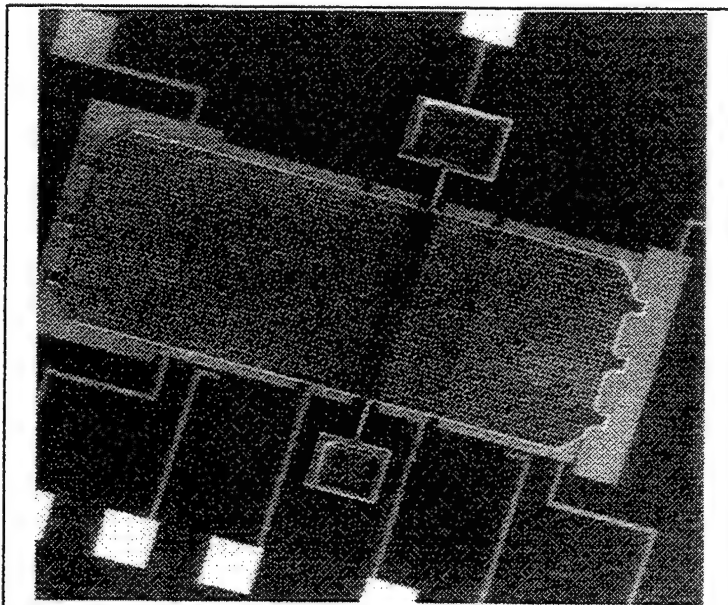


Figure 1.1 Draper Laboratory's Pendulous Mass Accelerometer

accelerometer mass. This seismic mass is constrained to move along the y-axis by six integral beams called accelerometer mass anchors. These anchors are designed to be stiff in the x and z-axis directions while flexible in the y-axis or acceleration input axis direction. This flexibility along the input axis allows a large percentage of an input load to be transferred to the oscillator's flexures. This input causes an axial load, either tension or compression, in the resonating oscillator beams which produces a measurable natural frequency shift of the two oscillators. The SOA takes advantage of common mode error rejection by incorporating the two oscillators. The frequency output of the two oscillators exhibits a differential shift under input acceleration. This frequency shift is measured and is proportional to an acceleration acting on the seismic mass which created the input load. Using frequency count as output from the device makes these units inherently digital so that integration with digital circuitry is simplified [9].

Interfacing with military and commercial avionics as well as with personal navigation instrumentation thus does not require analog-to-digital conversion or frequency-to-voltage conversion with their associated intrinsic errors.

The individual oscillators consist of two integral silicon masses with each mass supported by four flexures; two flexures on each side, as shown in figure 1.2. The flexures are integral with the oscillating masses on one side and are built into a beam, called a base beam, on the other side. Both sides of the oscillating masses have built in electrostatic drive and sense comb teeth. These teeth engage similar stationary comb teeth built into the anchored silicon electrostatic components. These electrostatic components are used to drive the two oscillator masses in an out-of-phase resonance as well as to sense the oscillator mass motion. The oscillator mass motion is sensed to both

sustain resonance via feedback and to determine oscillation frequency. The motion of the electrostatically forced out-of-phase mode of the oscillator masses is directed along the x-axis or motor drive and sense axis as labeled in figure 1.2. Because this out-of-phase, or tuning fork, resonance of the oscillators produces no net reaction force, the oscillators are said to be dynamically balanced. The individual oscillators with electrostatic drive and sense and automatic gain control (AGC) electronics are similar to those in Draper Laboratory's tuning fork gyroscopes [10]. An advantage of this electrostatic drive and sense comb teeth capacitor arrangement is that required components are fabricated from the same boron-doped, single crystal silicon and using the same microfabrication procedures as the other silicon structures. This simplifies the fabrication by eliminating the need for complicated plating or deposition steps.

Each anchored silicon electrostatic component has an associated metalization run on the glass that extends to the perimeter of the silicon and terminates at a metalized bond pad. These metalized runs and bond pads serve to enable electrical contact to each of the anchored silicon electrostatic components. Each of the four corner accelerometer mass anchors also have an associated metal run and bond pad for the purpose of electrically grounding the silicon structure. The remainder of the exposed glass surface under the silicon structure has been metalized to act as a grounded metallic shield plate. The overall dimensions of the device are approximately 3,400 x 3,400 x 780 microns. The schematic shown in figure 1.2 does not depict the perforations in the seismic and the oscillating masses designed to aid in fabrication and control out-of-plane damping. This schematic is not drawn to scale but shows the relative location and orientation of all

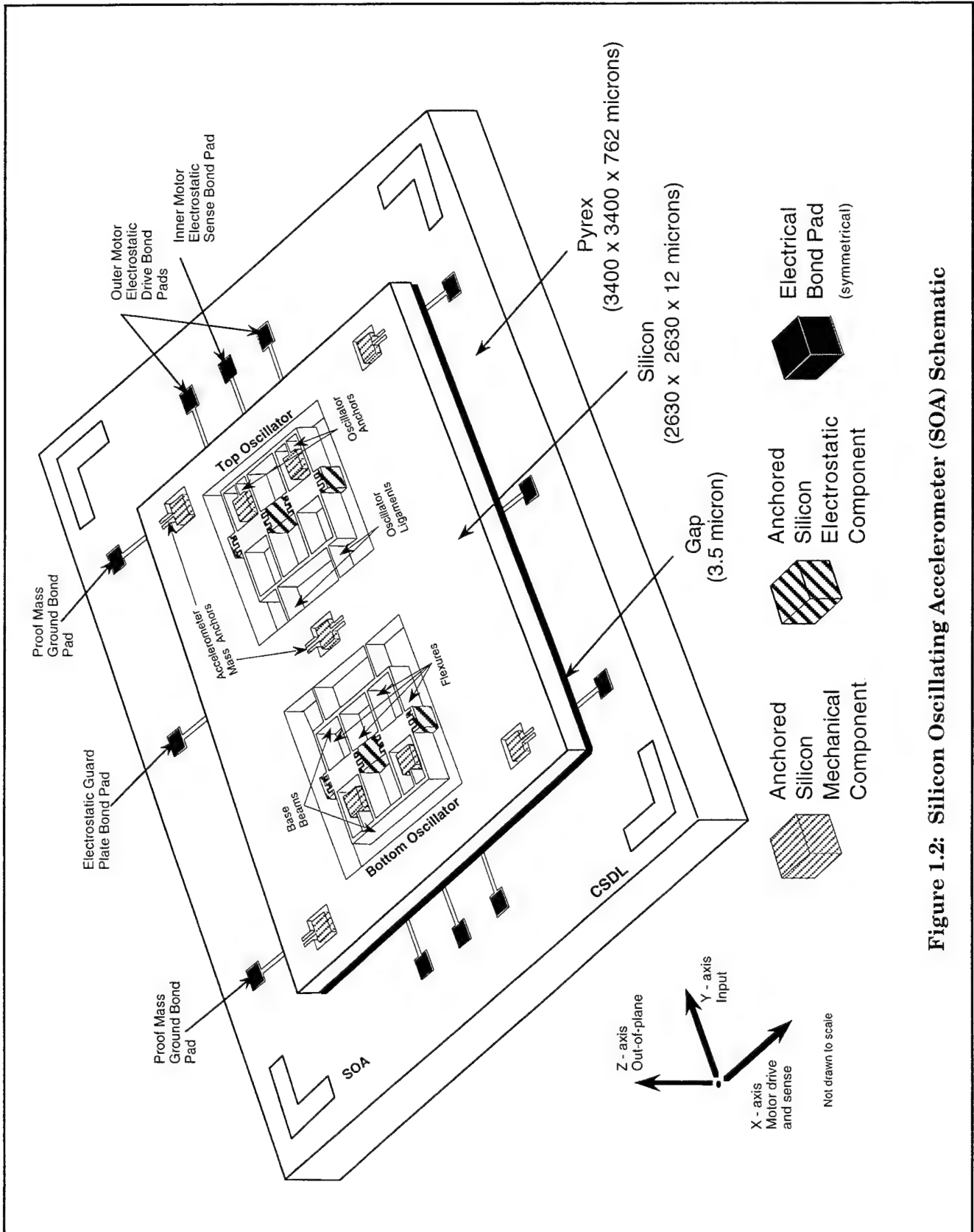


Figure 1.2: Silicon Oscillating Accelerometer (SOA) Schematic

dominant features of the accelerometer. These dominant features include: the two oscillators with associated vibrating beams, base beams, and oscillating masses, the large seismic accelerometer mass, the accelerometer mass anchor beams, and all bond sites between the silicon structure and the glass base.

2.0 BACKGROUND

2.1 Theory of operation

As shown in figure 1.2, the SOA can be divided into three major components; a seismic accelerometer mass made of silicon suspended between two silicon oscillators. The two tuning fork resonators sense acceleration through changes induced in their natural oscillation frequencies by acceleration of the seismic accelerometer mass.

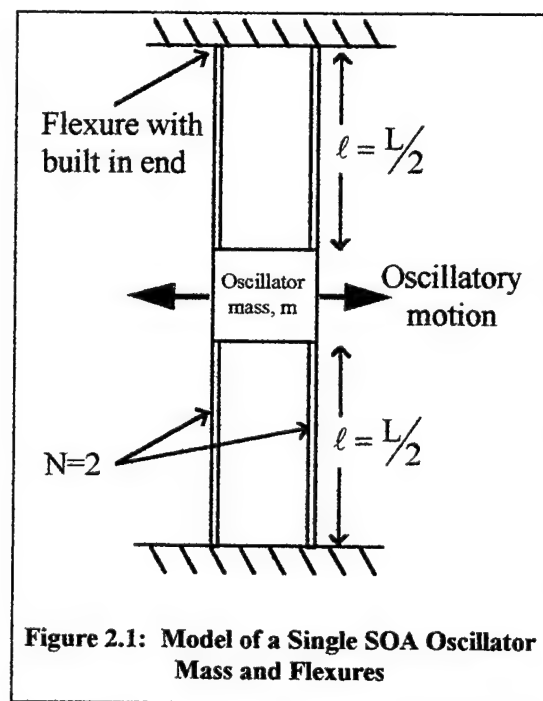
Input acceleration experienced by the SOA seismic mass causes loading in oscillators vibrating beams which run parallel to the input direction. The configuration of the two oscillators causes the accelerating seismic mass to load one oscillator's beams in tension while at the same time loading the other oscillator's beams in compression. The tensile loading of the beams of one resonator increases the oscillator's natural frequency. Similarly the compressive loading of the beams of the other resonator cause its resonant frequency to decrease. The difference of the resonant frequencies of the two oscillators is thus a measure of the acceleration of the base of the SOA along the input axis direction.

By differencing the natural frequency outputs from the two oscillators, the frequency shifts caused by effects common to both oscillators are removed. Employing this common mode subtraction or rejection technique greatly reduces such frequency shifting effects as temperature, nonlinearity of oscillation, off-axis accelerations, and aging. Because perfectly matched oscillators are difficult to fabricate, the common mode rejection effect is not total. Common mode rejection of ninety percent of the frequency shift caused by effects common to both oscillators will be assumed for analysis in this thesis.

Measuring the relative frequency shift between the two resonators, instead of absolute frequency also eliminates the necessity for a precise, high-frequency electrical voltage reference or clock. Differencing the frequency outputs can also be viewed as doubling the sensitivity of the instrument since the natural frequency shift of the two oscillators due to input acceleration are always in opposite directions.

Modeling of the oscillator for closed-form analysis

The two SOA oscillators are shown in figure 1.2. Each oscillator can be divided into two oscillating silicon masses and silicon flexure beams that support the two masses during oscillation. Each of the individual vibrating masses of the SOA oscillator can be



modeled as a mass suspended by four built-in flexible cantilever beams as shown in figure 2.1.

The cantilevers are of the left-end-guided and right-end-fixed type, as described by Roark & Young [11]. Table 11, entitled "Shear, moment, slope, and deflection formulas for beams under simultaneous axial tension and transverse loading" of Roark & Young provides a deflection equation, repeated here as (2.1), which gives deflection as a function of axial and transverse loading, beam geometry, and material constants.

$$X = \frac{-F}{KP} \left(\frac{C_3 C_{a3}}{C_2} - C_{a4} \right) \quad (2.1)$$

where X = the beam deflection,

P = the axial tensile load in the cantilever beam,

F = the transverse bending load,

E = Young's Modulus of Elasticity,

I = the area moment of inertia,

$K = (P/EI)^{1/2}$,

$C_2 = \text{Sinh}(K\ell)$,

$C_3 = \text{Cosh}(K\ell) - 1$,

$C_{a3} = \text{Cosh}(K\ell) - 1$,

$C_{a4} = \text{Sinh}(K\ell) - K\ell$, and

ℓ = cantilever beam length.

Substituting $\ell = L/2$; where L is the double cantilever beam length, into (2.1) and rearranging gives the beam stiffness for one beam as

$$K_{\text{beam}} = \frac{F}{X} = \frac{KP}{\frac{2}{\tanh(KL/2)} - \frac{2}{\sinh(KL/2)} - KL/2} \quad (2.2)$$

Then for 2N beams,

$$K_{\text{beams}} = \frac{2NKP}{\frac{2}{\tanh(KL/2)} - \frac{2}{\sinh(KL/2)} - KL/2}, \quad (2.3)$$

where N = the number of beams on one side of the oscillating mass.

Substituting $K = (P/EI)^{1/2}$ and performing a Taylor series expansion around $P=0$ gives

$$K_{\text{beams}} = \frac{F}{X} = \frac{192EIN}{L^3} + \frac{24NP}{5L} - \frac{LNP^2}{700EI} + \dots \quad (2.4)$$

This Taylor series expansion was performed in Macsyma version 2.1 commercially available symbolic mathematics software. Truncating to first order terms and rearranging (2.4) produces

$$K_{\text{system}} = \frac{F}{X} = \frac{192EIN}{(L)^3} + \frac{24PN}{5(L)}. \quad (2.5)$$

Taking the mass-spring-damper system of the oscillator, as shown in figure 2.2, to be second order, the resonant or natural frequency of the system is given by

$$\omega_n = \sqrt{\frac{K_{\text{system}}}{m}} \quad (2.6a)$$

and the quality factor, Q, for small values of damping [12] is given by.

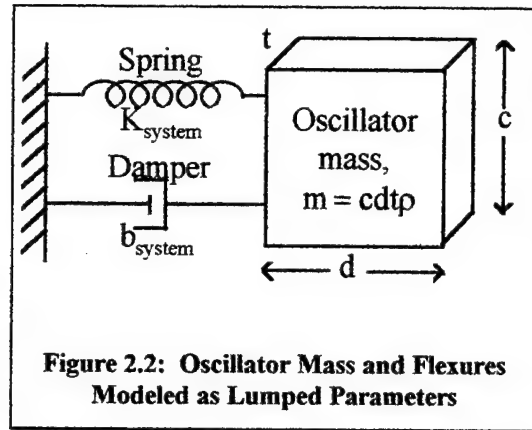
$$Q = \frac{1}{2\xi} = \frac{K_{\text{system}}}{b_{\text{system}} \omega_n} \quad (2.6b)$$

where ω_n = the system undamped natural frequency,

Q = the system quality factor or amplitude ratio at resonance,

ξ = the damping ratio, and

b_{system} = the system damping coefficient.

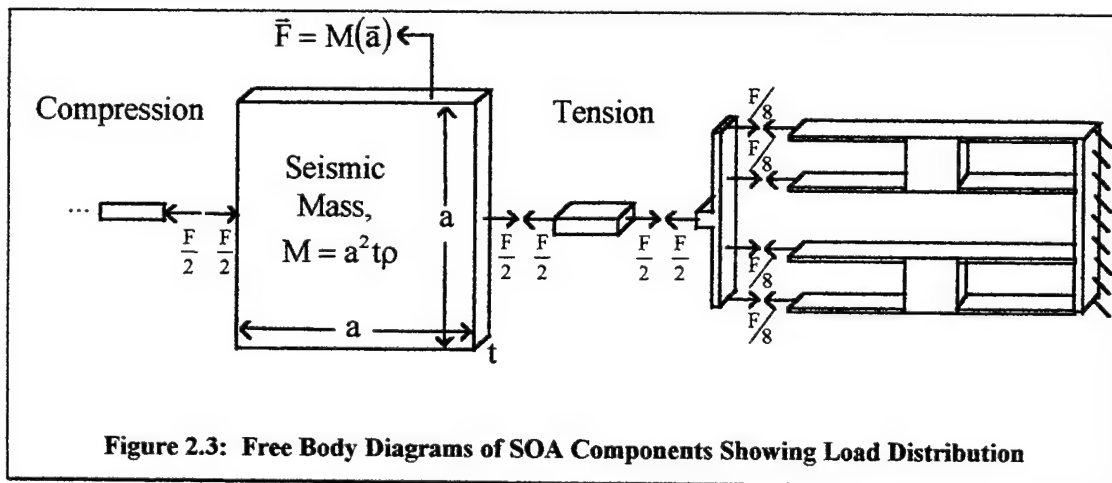


Substituting $N=2$ for two beams per oscillator mass side, $P=F/8$ as shown in figure 2.3, and mass as volume times density into (2.5) and then into (2.6a) produces

$$\omega_n = \sqrt{\frac{\frac{384EI}{L^3} + \frac{1.2F}{L}}{cd\rho}} \quad (2.7)$$

where c = the width,

d = the length,



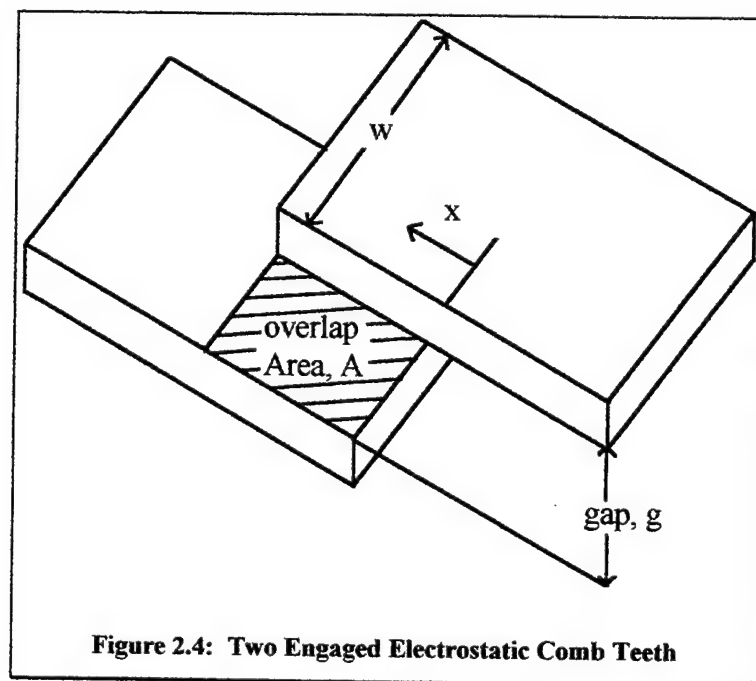
t = the thickness, and

ρ = the density of silicon; all of the oscillating mass.

Equation (2.7) is an expression for the resonant frequency of the oscillators of the SOA with axial loading [13].

Electrostatic forcing of the oscillator

Motion of the oscillator masses is accomplished using a capacitive forcing drive scheme in the form of overlapping or engaged capacitive comb teeth excited with a sinusoidally varying voltage signal and a constant bias voltage. This arrangement produces an electrostatic force. The perpendicular gap distance between comb teeth remains constant but the amount of comb tooth overlap varies from the nominal overlap with oscillator motion. Figure 2.4 shows two comb teeth, one associated with a fixed



electrostatic bond pad and the other with the moving oscillator mass. The electrical energy stored by this interaction of capacitive plates is

$$W = \frac{1}{2} CV^2 \quad (2.8)$$

where W = electrical work,

C = the plate capacitance, and

V = the potential difference between the plates [14].

The plate capacitance, C , is defined as

$$C = \frac{\epsilon A}{g} = \frac{\epsilon wx}{g}, \quad (2.9)$$

where ϵ = permittivity,

A = overlapping area, written as plate width times plate overlap; wx , and

g = the perpendicular plate gap distance.

Substituting (2.9) into (2.8) gives an expression for work as a function of plate geometry and drive voltage,

$$W = \frac{1}{2} \frac{\epsilon wx}{g} V^2. \quad (2.10)$$

The drive voltage, V , is composed of a constant voltage, V_{DC} , with a superimposed sinusoidal signal, $V_{AC} \sin \omega t$, and thus written as

$$V = V_{DC} + V_{AC} \sin \omega t.$$

Squaring this drive voltage gives

$$V^2 = (V_{DC} + V_{AC} \sin \omega t)^2$$

$$V^2 = V_{DC}^2 + V_{AC}^2 \sin^2 \omega t + 2 V_{DC} V_{AC} \sin \omega t$$

$$V^2 = V_{DC}^2 + V_{AC}^2 \left[\frac{1 - \cos 2\omega t}{2} \right] + 2V_{DC} V_{AC} \sin \omega t$$

$$V^2 = V_{DC}^2 + \frac{V_{AC}^2}{2} + \frac{V_{AC}^2}{2} \cos 2\omega t + 2V_{DC} V_{AC} \sin \omega t. \quad (2.11)$$

Substituting (2.11) into (2.10) gives

$$W = \frac{\epsilon w x}{2g} \left[V_{DC}^2 + \frac{V_{AC}^2}{2} + \frac{V_{AC}^2}{2} \cos 2\omega t + 2V_{DC} V_{AC} \sin \omega t \right]. \quad (2.12)$$

The electrostatic attractive force produced by these two overlapping capacitive plates along the x direction as shown in figure 2.4, is the first derivative of work with respect to the plate overlap, x . This force is given by

$$F_{\text{per edge}} = \frac{dW}{dx},$$

$$F_{\text{per edge}} = \frac{\epsilon w}{2g} \left[V_{DC}^2 + \frac{V_{AC}^2}{2} + \frac{V_{AC}^2}{2} \cos 2\omega t + 2V_{DC} V_{AC} \sin \omega t \right]. \quad (2.13)$$

Since the oscillator is driven at the natural frequency of the structure to achieve resonance, the terms in (2.13) that are at a frequency other than this resonant frequency are negligible contributors to the electrostatic force causing resonant motion. Since the first two terms in (2.13) are constants and since the third term drives at 2ω , twice the structure's natural frequency, these terms are not significant drive terms. The last term in (2.13), $2V_{DC}V_{AC}\sin\omega t$, does drive at the natural frequency of the oscillator, therefore it is the significant drive force term. Neglecting insignificant drive terms allows (2.13) to be reduced to

$$F_{\text{per edge}} = \frac{\epsilon w}{g} [V_{DC} V_{AC} \sin \omega t]. \quad (2.14)$$

The total electrostatic force produced by n active edges is thus given by

$$F_{\text{total}} = n \frac{\epsilon w}{g} [V_{\text{DC}} V_{\text{AC}} \sin \omega t], \quad (2.15)$$

where n = the total number of active capacitive edges or interfaces.

The electrostatic drive force result (2.15) is used in the preliminary mechanical design section, section 3.1, of this paper to predict electrostatic drive force. This estimated drive force amplitude is calculated to be 2.66×10^{-6} newtons peak for a two volt bias and one volt peak sinusoidal voltage.

Electrostatic sensing of the oscillator

Motion of the oscillator masses is sensed using capacitive comb teeth similar to those used in the capacitive drive scheme. An operational amplifier in a charge-to-voltage converter configuration is used to integrate the charge induced by the variations in sense comb capacitance as shown in figure 2.5. This sense comb capacitance is a function of tooth overlap and therefore a function of oscillating mass displacement just like the drive force capacitance.

Under ideal operational amplifier assumptions, the total output voltage [15] of the preamplifier in figure 2.5 is given by

$$V_{\text{so}} = V_{\text{sb}} + V_{\text{cfb}}.$$

Substituting for V_{cfb} gives

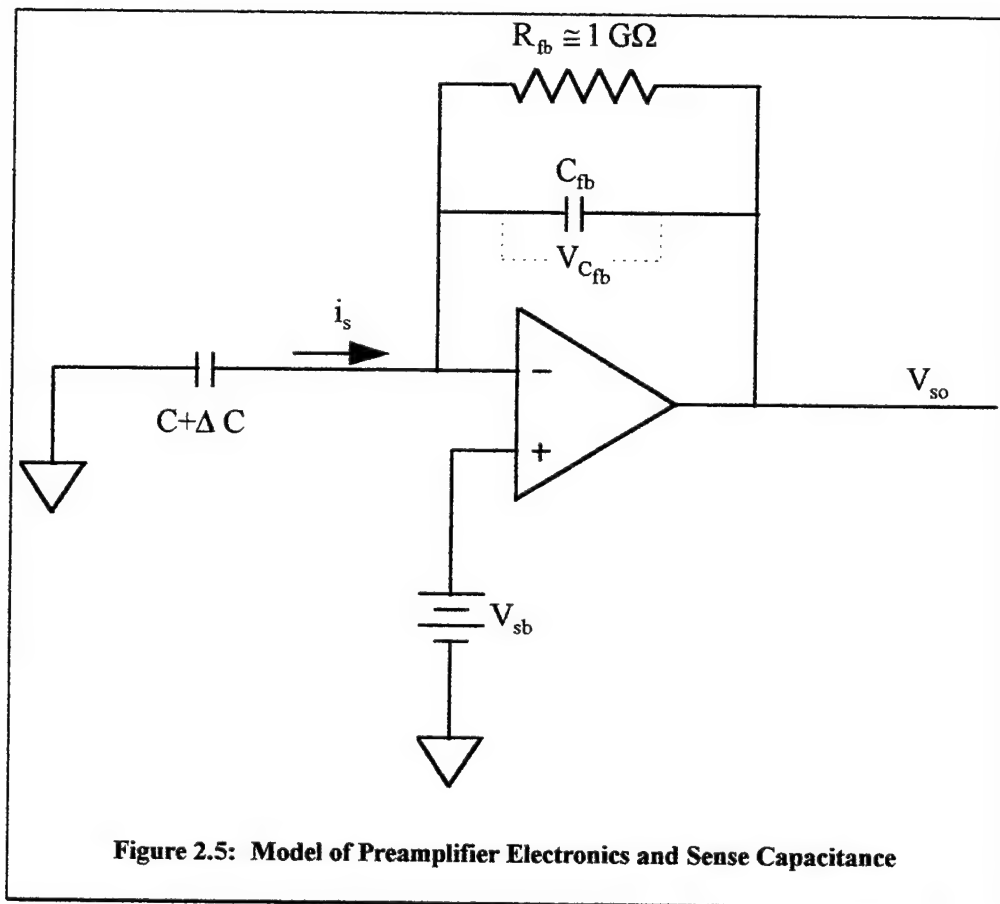
$$V_{\text{so}} = V_{\text{sb}} + \frac{q}{C_{\text{fb}}},$$

where q is the charge stored on C_{fb} . We assume that at the short time scales of interest, all of this charge, q , is sourced by the change, ΔC , in the sense capacitance. Thus

$q = \Delta C V_{sb}$ and therefore

$$V_{so} = V_{sb} + \frac{\Delta C V_{sb}}{C_{fb}}.$$

Two assumptions for this analysis are $C + \Delta C > 0$ and ΔC changes faster than the $R_{fb}C_{fb}$



time constant. Both assumptions hold since the electrostatic comb capacitance is always positive and since for a feedback resistance of $1\text{ G}\Omega$ and feedback capacitance of 2 pF , the time for ΔC to change at twenty five kilohertz is much less than the 2 msec RC time

constant. Therefore the incremental output voltage, V_{so}' , as a function of the sense bias voltage, V_{sb} , the feedback capacitance, C_{fb} , and the change in the sense comb capacitance, ΔC , is

$$V_{so}' = V_{sb} \frac{\Delta C}{C_{fb}}. \quad (2.16)$$

This result for sense output voltage in (2.16) will be used in the preliminary design feasibility calculations presented in section 3.1 of this thesis to calculate an estimated amplitude of the sinusoidal output voltage signal of 0.005 volts peak. The large feedback resistor in figure 2.5 is necessary to prevent integration of bias currents at the amplifier input.

Bias stability

The bias stability of the SOA is also an important characteristic. We define the SOA bias as the output difference frequency given no acceleration input. This bias value is determined by how closely the two oscillator frequencies match after microfabrication. If this bias value is reasonably stable, thus predictable, it can be removed from the output leaving a zero output for a no-acceleration input condition. Many factors can affect the SOA's bias stability. Two of these factors are thermal sensitivity and flexure stiffness nonlinearity. The effects of both of these factors are greatly reduced through common mode subtraction since they affect both oscillators simultaneously. Since common mode rejection is not perfect, as described earlier, it is important to minimize the magnitude of the effects by design, if possible, thereby keeping the signal to noise ratio as high as possible.

Thermal sensitivity

The thermal sensitivity effect is divided into two counteracting components. Thermal expansion of the Pyrex with increasing temperature places the silicon into tension since the thermal expansion coefficient of the glass is greater than that of silicon. This tension in the silicon acts to increase the natural frequency of the oscillators because the vibrating beam stiffness increases. This effect is discussed in the detailed mechanical design section, section 3.2, of this paper. Opposing this thermal expansion coefficient effect is the decreasing Young's modulus of silicon with temperature. The decrease of Young's modulus of silicon with increasing temperature acts to decrease the natural frequency of the oscillators since the vibrating beam stiffness decreases. Thus there exist anchor point locations and base beam geometry that allow the stretching of silicon effect on frequency to be countered with the decreasing Young's modulus of silicon effect on frequency with changing temperature. These optimum anchor point locations and base beam dimensions are the design point where the shift in oscillator natural frequency due to temperature effects is minimized.

From (2.7), the oscillator resonant frequency is shown to be proportional to the square root of Young's modulus of silicon as

$$\omega_0 = \psi \sqrt{E}, \quad (2.17)$$

where ω_0 = the nominal oscillation frequency,

ψ = a constant of proportionality, and

E = Young's modulus for silicon.

From (2.17), it follows that

$$\Delta\omega = \frac{1}{2}\psi E^{-1/2}\Delta E, \quad (2.18)$$

Dividing (2.18) by (2.17) and rearranging yields

$$\Delta\omega = \frac{1}{2} \frac{\Delta E}{E} \omega_0. \quad (2.19)$$

From (2.19), it is possible to calculate the expected shift in natural frequency given a shift in Young's modulus. This result of this calculation, -0.65 hertz per degree Celsius, was compared to the result of the frequency shift due to thermal expansion coefficient mismatch calculation as described in the detailed mechanical design section, section 3.2, of this thesis.

Flexure stiffness nonlinearity

The flexure stiffness nonlinearity effect on the natural frequency of the oscillator is approximated using Nayfeh and Mook's [16] solution to

$$\ddot{x} + \sum_{n=1}^N \alpha_n x^n = 0 \quad (2.20)$$

where $\sum_{n=1}^N \alpha_n x^n$ is a polynomial representation of a nonlinear spring.

Here

$$\alpha_n = \frac{1}{n!} f^{(n)}(u_0)$$

are the stiffness coefficients of the nonlinear spring where f is a nonlinear function representing spring force as a function of position x . Here $f^{(n)}$ denotes the n th derivative of force with respect to position. The location of the center of oscillation is u_0 and the

motion is oscillatory in the neighborhood of u_0 . For our purposes, we let $n = 3$, and thus have

$$\ddot{x} + \alpha_3 x^3 + \alpha_2 x^2 + \alpha_1 x = 0.$$

To solve (2.20), Nayfeh and Mook used the method of harmonic balance and assumed a three term solution

$$\omega = \sqrt{\alpha_1} \left[1 + \frac{9\alpha_3\alpha_1 - 10\alpha_2^2}{24\alpha_1^2} A_1^2 \right] + \dots, \quad (2.21)$$

where A_1 is the oscillation amplitude.

For $\sqrt{\alpha_1} = \omega_0$, $\alpha_2 = 0$ and neglecting higher order terms in A_1 , (2.21) becomes

$$\omega = \omega_0 \left[1 + \frac{3\alpha_3\alpha_1}{8\alpha_1^2} A_1^2 \right]. \quad (2.22)$$

By differentiating (2.22) with respect to A_1 and evaluating at A_{10} , produces

$$\left. \frac{d\omega}{dA_1} \right|_{A_1=A_{10}} = 2\omega_0 \frac{3}{8} \frac{\alpha_3}{\alpha_1} A_{10}. \quad (2.23)$$

Multiplying (2.23) by $\frac{A_{10}}{\omega_0}$ and rearranging gives

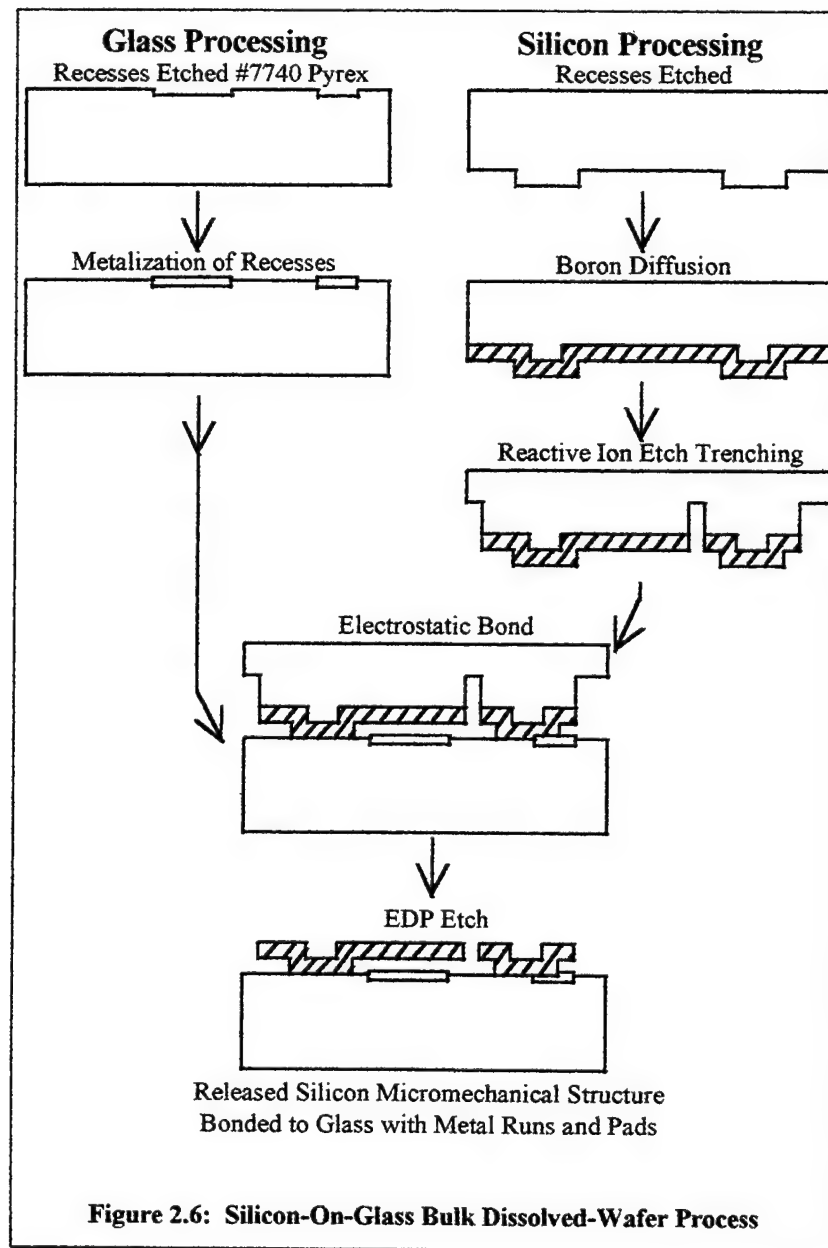
$$\Delta\omega = 2 \left(\frac{3}{8} \right) \left(\frac{\alpha_3}{\alpha_1} \right) A_{10}^2 \omega_0 \frac{\Delta A_1}{A_{10}}. \quad (2.24)$$

The result (2.24), shows the change in frequency that can be expected as a function of the flexure stiffness nonlinearity and the amplitude of oscillation. This result will be used later in the finite element analysis section, section 3.2, where the flexure stiffness nonlinearity is determined, to show that a 0.0013 hertz shift can be expected for an SOA oscillator resonating at a one micron oscillation amplitude. This is a negligibly

small shift, and thus we can readily model the flexures as a linear spring for such small amplitudes of vibration.

2.2 The microfabrication process

For micromachining inertial instruments, Draper Laboratory employs the silicon-



on-glass bulk dissolved-wafer process. The main process steps are illustrated in figure 2.6. This process has been used in other inertial sensor fabrication [8],[17].

The fabrication process starts by processing the glass (Pyrex) and silicon structure separately as described below. The process brings the glass and silicon together in later steps.

The glass processing involves photomasking and etching recesses on the #7740 Corning glass wafer surface. These recesses are subsequently filled with a metalization layer that protrudes slightly above the Pyrex glass surface. This metalization serves as a network of bond pads and electrical conductors used to operate the completed micromechanical device.

The silicon process begins with p-type single-crystal-silicon wafers. Potassium hydroxide is used to etch recesses in the preoxidized, photomasked, then deoxidized silicon. These recesses define the gap that will exist between the glass and silicon structure upon completion. The final silicon structure thickness is defined by the depth of a boron diffusion which acts as an etch stop and produces silicon structures that are good electrical conductors. Cuts in final silicon structure geometry are defined by another photomasked etch, a reactive ion etch (RIE).

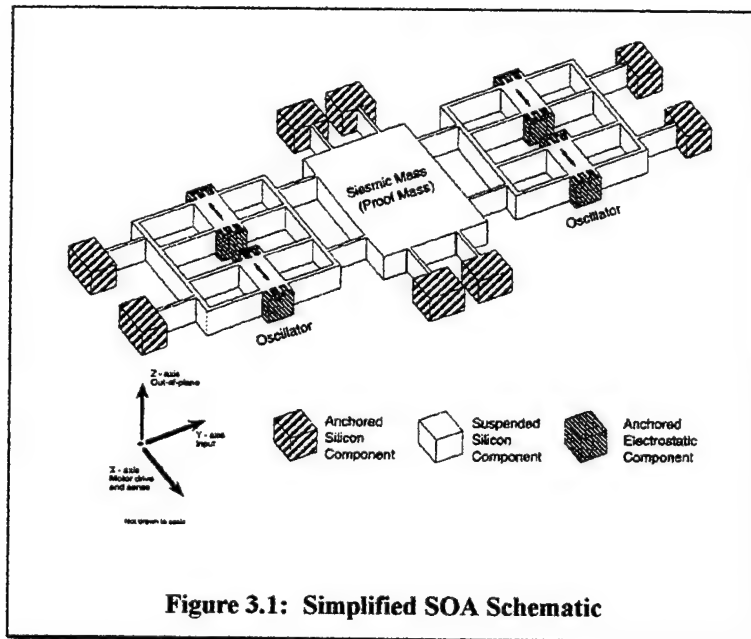
The glass and silicon wafers are sawn into tablets. The silicon and glass, both plain and metalized areas, are then intimately joined using a pressurized electrostatic bonding process. The next step is a selective chemical etch. The etchant, ethylene diamine pyrocatechol (EDP), removes only silicon that is not heavily boron doped, leaving the desired silicon structure bonded to the glass. Finally, the tablets are chopped into individual micromechanical devices that are ready for test.

This dissolved-wafer silicon-on-glass process is compatible with batch processing and is capable of high yield [10]. Several of Draper Laboratory's fabrication process issues impacted the SOA design in one way or another. These issues included limitation on overall instrument size to a square of approximately 3.5 millimeters per side including bond pads, limitation on thickness to twelve microns, minimum flexure beam width of 3.5 microns, and a maximum glass/silicon gap distance of 3.5 microns. Also perforating all silicon plate structures with an array of holes is required for proper fabrication. These perforations allow chemical etchants and solvents to flow easily through and around all areas of the silicon therefore washing used materials and debris away from the emerging and finished structure during processing.

3.0 DESIGN ANALYSIS

3.1 Preliminary mechanical design calculations

Preliminary design analysis was performed before finite element methods were used. This lumped parameter analysis was performed using a simple schematic shown in figure 3.1. This schematic shows the three essential components of the SOA; the two



oscillators and the seismic mass. The analysis was further simplified by assuming that the oscillator vibrating beams were built in at one end. In reality these beams are connected to other beams of the oscillator, named base beams, as marked in figure 1.2. These base beams decrease the overall stiffness by contributing some flexibility to the system which acts to decrease the system resonant frequencies. This simplification served quite well for preliminary design analysis even though it resulted in a larger value for stiffness and thus natural frequency of the oscillator than the finite element analysis

where this simplification was not used. The finite element analysis is described in the detailed mechanical design section, section 3.2, of this thesis.

This preliminary analysis served to determine feasibility of the SOA concept. The type of closed-form analysis used in the preliminary design stage is important in understanding approximate relationships between geometry, frequency, and sensitivity of the SOA. It is also crucial as an independent analysis comparison for future, more involved and detailed analysis.

The SOA preliminary analysis was coded into a Microsoft Excel 5.0 spreadsheet. Appendix A contains a hard copy of this spreadsheet with the variable names and equations included. This spreadsheet contains the required silicon material properties used in this analysis and values of other required constants. Single crystal silicon has a diamond cubic lattice geometry with orthotropic properties. For sufficiently slender beams, only Young's modulus along the length of the beams affect stiffness [18]. For the analysis presented here, the assumed isotropic Young's modulus for silicon is $1.65 \times 10^{11} \text{ N/m}^2$ [19] which describes beams parallel to the $\langle 110 \rangle$ silicon lattice direction. This value provided sufficient accuracy since the SOA vibrating beams were fabricated along this $\langle 110 \rangle$ lattice direction. For later analysis, the temperature dependence of Young's modulus was taken as $-122 \text{ ppm/}^\circ\text{C}$ from Metzger and Kessler [20]. Subsequent work shows that $-52 \text{ ppm/}^\circ\text{C}$ is a value produced from more reliable experimentation [21]. The thermal expansion coefficient of silicon was taken as $2.3 \times 10^{-6}/^\circ\text{C}$ [22] and that of Pyrex as $3.25 \times 10^{-6}/^\circ\text{C}$ as shown in Appendix B. Later the thermal expansion coefficient for silicon was updated to the room temperature value of

$2.6 \times 10^{-6}/^{\circ}\text{C}$ therefore making the thermal expansion coefficient mismatch between the silicon and glass equal to $6.5 \times 10^{-7}/^{\circ}\text{C}$.

Equations (2.5) and (2.7) as developed in the theory of operation section, section 2.1, of this thesis along with material property data were used in the preliminary design spreadsheet. These equations were used to calculate oscillator beam stiffness and an oscillator resonant frequency given various geometry variations and no axial loading.

The oscillator natural frequency was calculated for the case in which a one g acceleration along the input axis of the SOA causes a tensile loading in the oscillator vibrating beams. This frequency could then be compared to the no load resonant frequency to calculate an estimated scale factor or input axis acceleration sensitivity. An instrument scale factor of 2.3 hertz per g was calculated.

The results of the spreadsheet calculations are shown in figures 3.2 through 3.6. Figure 3.2 shows a near linear increase in oscillator resonant frequency with vibrating flexure width. A design objective is to have the out-of-phase oscillation frequency, or operating frequency, near twenty five kilohertz. This aids in ensuring compatibility with an existing AGC electronics design. From figure 3.2, a vibrating flexure width from approximately three to five microns will meet the operating frequency requirement. The SOA scale factor versus vibrating flexure width curve, in figure 3.4, shows that narrow beam widths maximize the scale factor. Since the narrowest beam width was limited to four microns by the current fabrication process, four microns was thus chosen as the baseline flexure width. After choosing the flexure width and examining figure 3.3, an oscillating mass width of 150 microns was selected to keep a 25 kHz operating frequency. Even though figure 3.5 shows that a smaller oscillating mass width would

produce an increased scale factor, the constraint of frequency compatibility with existing electronics fixed the width to 150 microns. Figure 3.6 shows that as the size of the seismic mass of the accelerometer, assumed here to be square, increased, the instrument scale factor increased as this side dimension, a , squared. Appendix C contains the data shown in figures 3.4, 3.5, and 3.6 as $\Delta F/F/g$ instead of Hz/g.

The electrostatic force equations, (2.14) and (2.16), developed in the theory of operation section, section 2.1, were used in the design spreadsheet to estimate electrostatic drive and sense parameters. Table 3.1 contains some of the resulting estimated values for electrostatic parameters. Some calculation input parameters, such as thirteen moving and fourteen fixed electrostatic comb teeth per capacitor, are also shown in table 3.1. See Appendix A for other values.

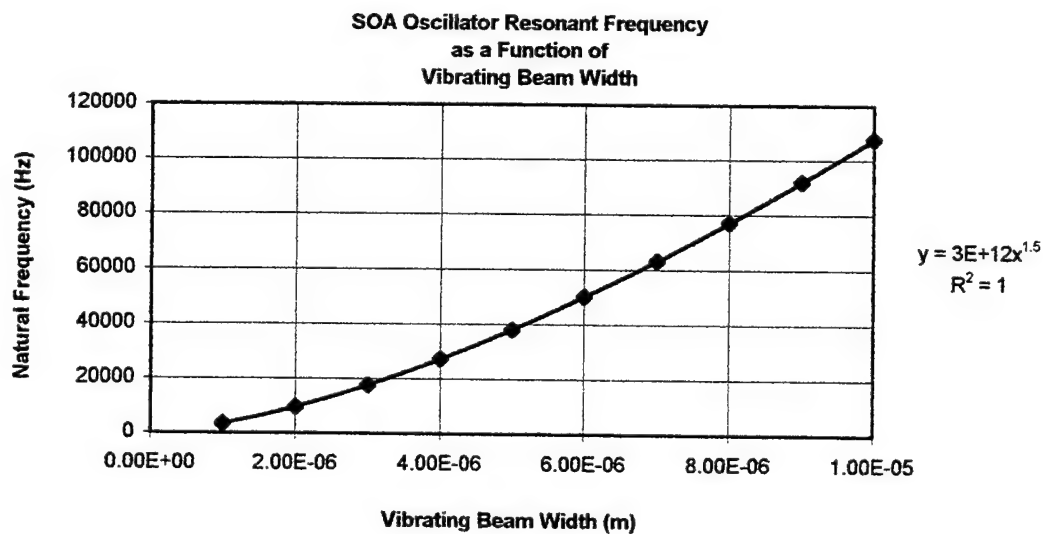


Figure 3.2: Preliminary Design Natural Frequency versus Beam Width

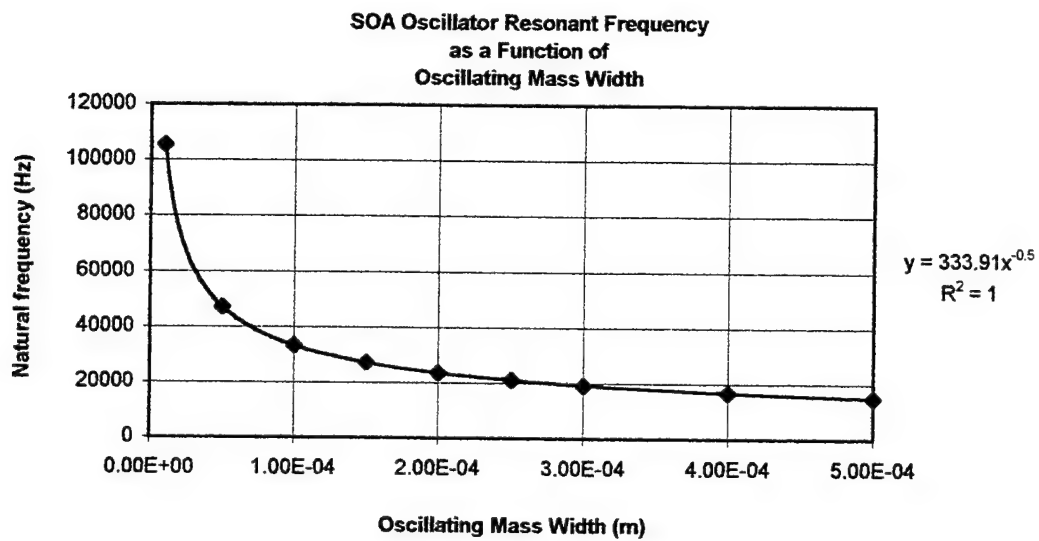


Figure 3.3: Preliminary Design Natural Frequency versus Oscillating Mass Width

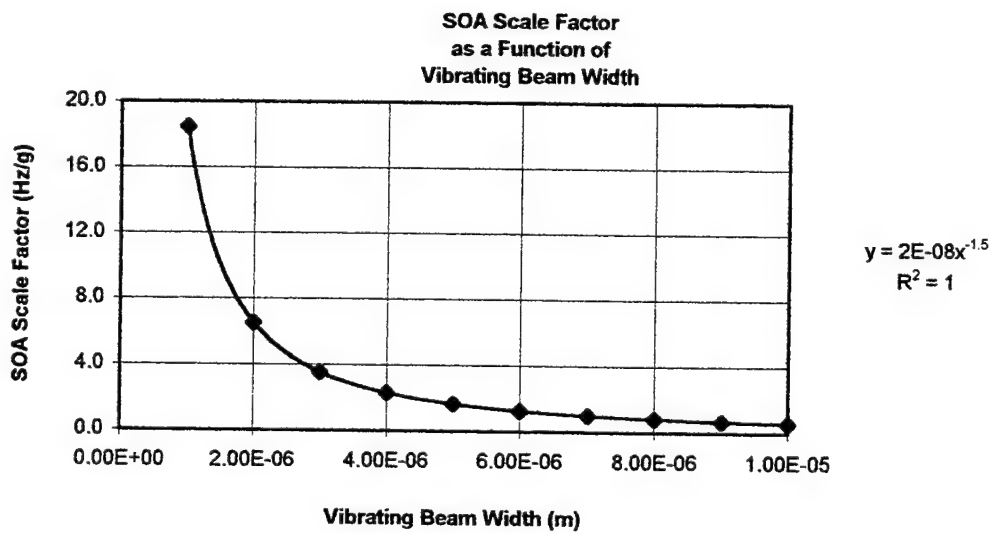


Figure 3.4: Preliminary Design Scale Factor versus Beam Width

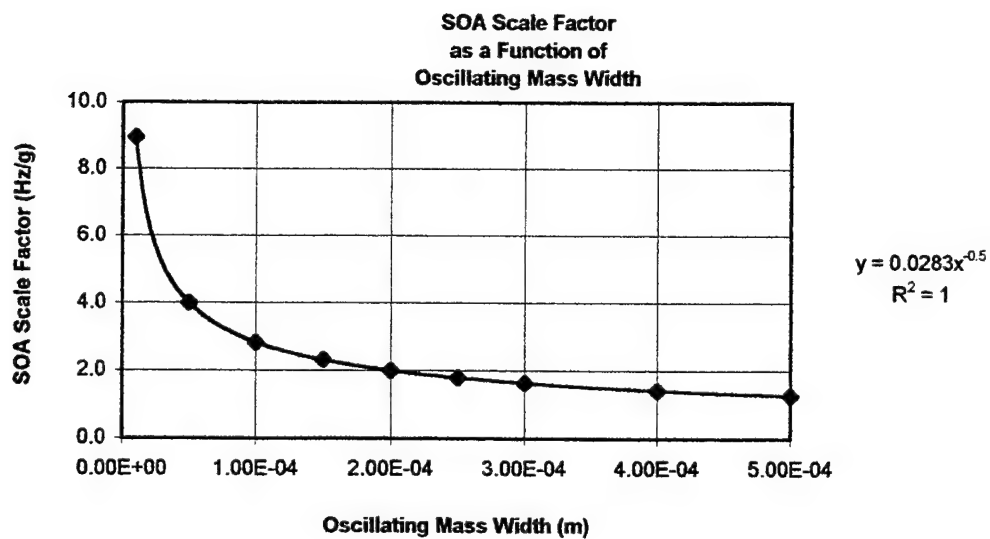


Figure 3.5: Preliminary Design Scale Factor versus Oscillating Mass Width

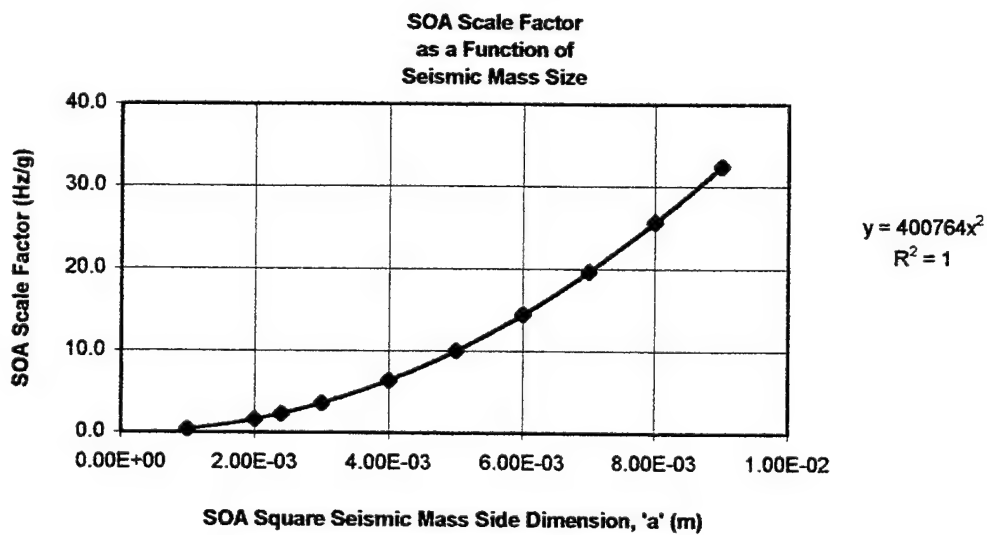


Figure 3.6: Preliminary Design Scale Factor versus Seismic Mass Width, a

With the listed estimated inputs, the amplitude of the sinusoidal output voltage

Electrostatic Parameter	Value	Units
Number of Moving/Fixed Comb Teeth per Capacitor *	13/14	
Width of Comb Teeth *	4	microns
Length of Comb Teeth *	16	microns
Gap between Comb Teeth *	2	microns
Thickness of Comb Teeth *	12	microns
Drive Bias Voltage *	2.0	volts
Drive Amplitude Voltage *	1.0	volts (peak)
Electrostatic Force Amplitude	2.66×10^{-6}	newtons (peak)
Comb Displacement *	1.0×10^{-6}	meters (peak)
Sense Capacitance Coefficient	1.33×10^{-9}	farads/meter
Sense Bias Voltage *	5.0	volts
Output Voltage Signal	0.005	volts (peak)
* Calculation input value		

Table 3.1: Estimated Electrostatic Drive and Sense Parameters

signal from the sense preamplifier as shown in figure 2.5, is 5 millivolts peak, a value of sufficiently high magnitude.

This preliminary closed form spreadsheet analysis and the results presented in this section showed that the SOA was a theoretically viable concept and that this concept merited the additional investment of detailed mechanical design presented in the next section of this paper. This closed form analysis would later serve as a comparison for detailed numerical analysis results. The detailed analysis results should compare to these closed form calculations by producing at least similar order-of-magnitude results to increase confidence that proper understanding of dominant physical phenomena has been achieved.

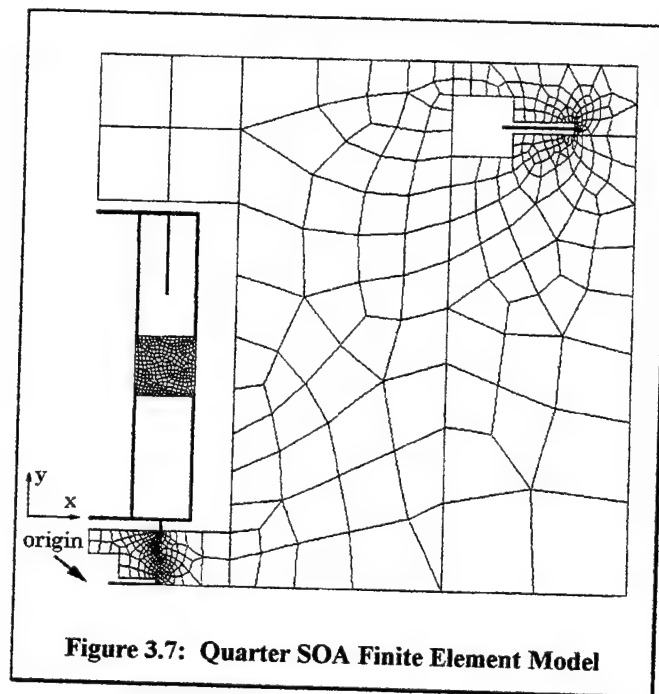
3.2 Detailed mechanical design

The SOA detailed design analysis simulations were performed using the commercially available ANSYS version 5.2 finite element software [23]. The first finite element simulation involved developing and analyzing a quarter finite element model of the SOA.

The SOA quarter model analysis was performed using the finite element model shown in figure 3.7. This quarter model exploits both the horizontal or x-axis as well as vertical or y-axis geometric symmetry of the instrument. ANSYS Plane82, two dimensional, plane stress, eight node, structural solid elements were used in this analysis with a specified thickness. This element is explained in the Plane82 element section of the ANSYS User's Manual [24].

The same material properties for silicon discussed earlier in the preliminary design section of this paper were used in order to make these analyses comparable with the preliminary spreadsheet analysis.

The geometry for the quarter model was entered into ANSYS by inputting key points in Cartesian coordinates. These key points were then used to form areas. The auto-meshing routine in ANSYS was employed to operate on the set of areas to produce a



mesh of nodes and finite elements as shown in figure 3.7. The model contained 4,018 nodes and 1,198 elements. Five separate analyses were run on this model. Separate analyses were required to determine the out-of-phase oscillation mode frequency, the in-phase oscillation mode frequency, the out-of-phase oscillation mode frequency under a one g preload along the input axis (y-axis), the out-of-phase oscillation frequency for a

temperature sensitivity baseline, and finally the out-of-phase oscillation frequency under set anchor point displacements to approximate temperature sensitivity. Each of these analyses were carried out on the quarter model with appropriate symmetry and asymmetry boundary conditions as described here.

Out of phase oscillation frequency determination

To determine the out-of-phase oscillation mode frequency, which is the operating frequency of the instrument, a symmetry boundary condition was assigned to all nodes lying on the y-axis. An asymmetry boundary condition was assigned to all nodes lying on the x-axis for comparison purposes with a later analysis. Nodes along the three lines fixed at anchor points were constrained to zero displacement in both x and y directions. A linear model analysis was then performed using a subspace iteration to solve the eigenvalue problem

$$[K]\{\phi_i\} = \lambda_i[M]\{\phi_i\} \quad (3.1)$$

where $[K]$ = the structure stiffness matrix,

$\{\phi_i\}$ = the eigenvector,

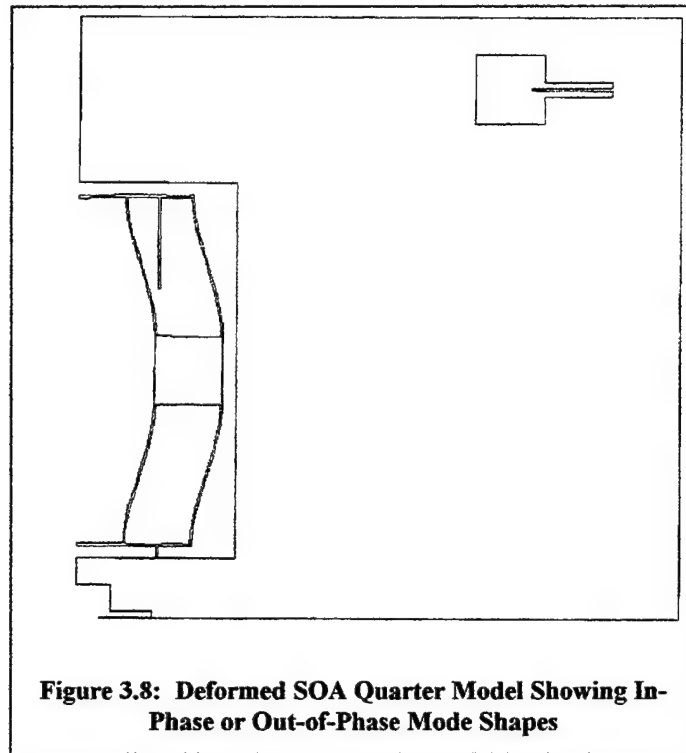
$[M]$ = the structure mass matrix, and

λ_i = the eigenvalue,

where $\lambda_i = \omega_i^2$ and ω_i is the modal frequency.

This method of subspace iteration is described in the ANSYS User's Manual [24].

The results of this analysis are the set of eigenvalues, and mode frequencies, and



a graphical representation of the associated eigenvectors or mode shapes. The mode shape displacements are normalized to one and scaled by a factor to enhance perception. Figure 3.8 is an example of the mode shape displacement plots. This figure shows a deformed SOA quarter model displacement plot. The in-phase and out-of-phase mode shape displacement plots of the oscillator quarter model appear identical to figure 3.8. Given that a y-axis symmetry or asymmetry boundary condition was used in this quarter model analysis, this figure depicts the out-of-phase or in-phase oscillation mode, respectively. The set of eigenvalues and associated eigenvectors includes the number of values specified by the analyst that are compatible with the boundary conditions specified. Since the in-phase oscillation mode is not compatible with the y-axis

symmetry boundary conditions of the out-of-phase mode a separate analysis with the appropriate boundary conditions is required to determine this mode frequency.

In phase oscillation frequency determination

It was necessary to determine the in-phase oscillation frequency in order to satisfy a design objective to have all other oscillation mode frequencies at least ten percent away from the primary operating frequency. The primary operating frequency of the SOA oscillators is the out-of-phase resonant frequency.

For the in-phase frequency analysis a y-axis asymmetry boundary condition was used, the x-axis remained an asymmetric boundary condition. The nodes with fixed zero displacements at the anchor points in the out-of-phase frequency determination remained fixed and the modal analysis repeated. The results again are a set of eigenvalues and eigenvectors shown as displaced geometry with displacements normalized to one.

Input acceleration sensitivity determination

The next analysis was necessary to determine the sensitivity of the design to acceleration along the input axis of the instrument. The quarter model of the SOA was again used with y-axis symmetry and x-axis asymmetry boundary conditions, exactly like the out-of-phase oscillating frequency determination so that direct comparison could be made. This analysis was performed in two stages. The first stage was a static analysis with 9.8 m/s^2 , one g, linear acceleration along the input axis or y-axis, applied to determine the element loading produced by this acceleration. This loading is asymmetric about the x-axis, thus the reason for the x-axis asymmetry boundary condition. The

results of the static analysis were then used to prestress the structure before running the second stage of the analysis. The second stage was then identical to that described in determining the out-of-phase frequency without preload. The result was the eigenvalue associated with the out-of-phase oscillation mode when the instrument is subjected to one g acceleration along the input axis. From this data, an instrument sensitivity, or differential frequency scale factor, of 4.0 hertz per g was calculated for the two oscillators.

Thermal effects determination

The final two simulations, using the SOA quarter model, were to assess the effect of the silicon and glass thermal expansion coefficient mismatch on the oscillation frequency of the instrument; first a baseline case then a preloaded, elevated temperature simulation.

The baseline case had nodes on the x-axis and y-axis set to symmetry boundary conditions to be compared to the next case, the temperature preload case.

To simulate temperature effects due to stretching of silicon by the Pyrex substrate, the amount of individual anchor point displacement in the x and y directions was calculated and used as a fixed displacement to which the nodes at the anchor points were constrained. For example, anchor point displacement was calculated by taking the product of (1) the difference of the thermal expansion coefficients of Pyrex and silicon, (2) distance of the anchor point from the origin, as shown in figure 3.7, and (3) a temperature shift in degrees Celsius. A linear static analysis was performed with these fixed displacements and element stresses were calculated. These static analysis results

Flexure width	Base beam width	Out-of-Phase frequency	In-Phase frequency	y-axis 1 g loading	Temp baseline	10 °C temp. stretch
microns	microns	Hz	Hz	Hz	Hz	Hz
3.5	4	20,069.3	17,746.2	20,071.2	20,066.2	20,072.4
4.0	4	23,790.1	20,000.6	23,791.7	23,787.2	23,792.9
4.5	4	27,427.9	22,017.0	27,429.3	27,425.5	27,430.9
3.5	6	20,856.4	18,762.8	20,858.7	20,847.4	20,864.5
4.0	6	25,075.2	21,564.6	25,077.2	25,068.4	25,083.1
4.5	6	29,385.2	24,008.6	29,386.9	29,379.2	29,392.2
3.5	8	21,053.6	19,089.4	21,056.1	21,070.7	21,107.3
4.0	8	25,481.3	22,111.0	25,483.3	25,449.9	25,480.8
4.5	8	30,011.1	24,828.1	30,012.8	29,997.2	30,024.0

Table 3.2: FEA Modal Results for Three Flexure Widths and Three Base Beam Widths

were used to prestress the structure before running the modal analysis. The result was the out-of-phase oscillation frequency with the silicon preloaded due to stretching of the silicon by the Pyrex to which it is bonded. This frequency was compared to the baseline temperature case to determine how much the frequency would shift due to this thermal expansion mismatch of the silicon and Pyrex over a one degree Celsius temperature increase.

These results were compared to the calculated frequency shift due to the change of Young's modulus of silicon per the same one degree Celsius temperature shift. This balancing effect between stretching and softening of silicon was described in the theory of operation section, section 2.1. This combined effect gives an estimate of the temperature sensitivity of the SOA oscillator in hertz per degree Celsius. It was desirable to minimize this combined temperature effect since common mode rejection is not perfect for oscillators that are not identically fabricated.

For the four micron flexure width and six micron base beam design the frequency shift of the oscillator due to the thermal expansion coefficient mismatch of the glass and silicon was calculated to be $1.03 \text{ Hz}/^{\circ}\text{C}$ from the finite element analysis results shown in table 3.2. The opposing frequency shift due to the change in the Young's modulus of silicon with temperature is calculated using (2.19) to be $-0.65 \text{ Hz}/^{\circ}\text{C}$. Therefore the net frequency change due to temperature is $0.38 \text{ Hz}/^{\circ}\text{C}$. This value was used along with the assumptions of 0.01°C temperature control, an instrument scale factor of 4.0 Hz/g , and a factor of ten common mode rejection, to produce a calculated instrument bias stability of approximately one hundred micro-g's due to temperature sensitivity if temperature is held to 0.01°C .

Finite element analysis results for the in-plane element, quarter SOA model

The results for the in-plane element, quarter model, mode analyses for various base beam and oscillating beam widths are tabulated in table 3.2. Graphs of this data are shown in figures 3.9 through 3.11.

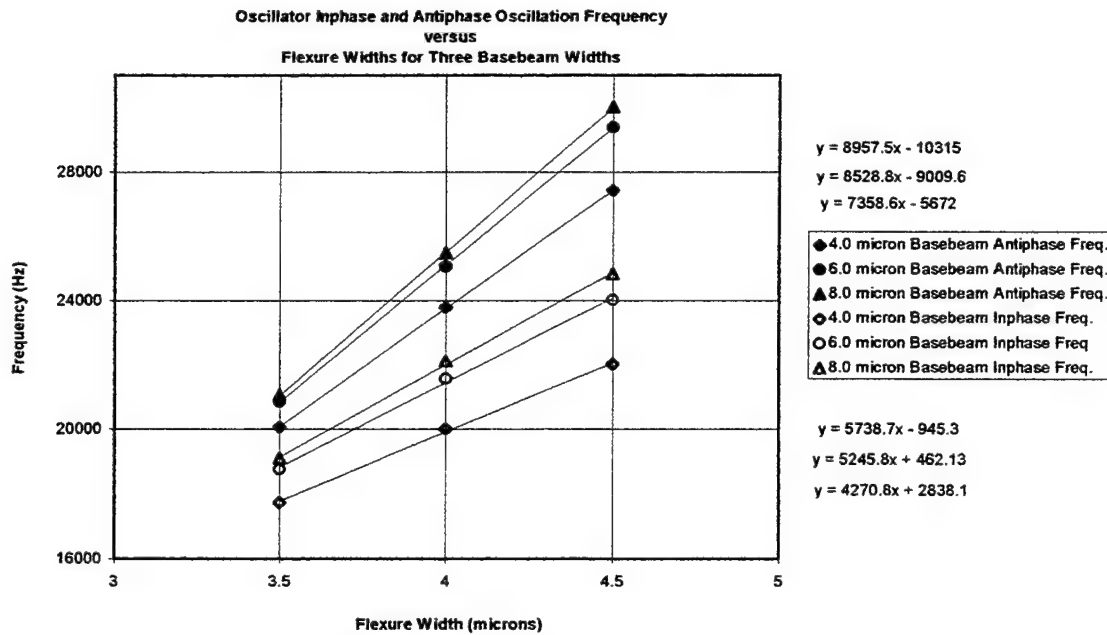


Figure 3.9: SOA FEA Natural Frequencies versus Flexure Width

Figure 3.9 displays the out-of-phase and in-phase oscillator frequencies, as determined by finite element methods, as a function of vibrating beam and base beam width. This figure shows that as flexure width decreases, the out-of-phase and in-phase frequencies converge for all base beam widths.

SOA scale factor is displayed in figure 3.10 as a function of vibrating flexure width and base beam width. This figure shows that scale factor decreases with both increasing flexure width and decreasing base beam width.

Figure 3.11 shows the results of the steady state temperature sensitivity analysis performed as described earlier with the thermal expansion coefficient of silicon of $2.3 \times 10^{-6}/^{\circ}\text{C}$ and the change of Young's modulus of silicon with temperature of -122

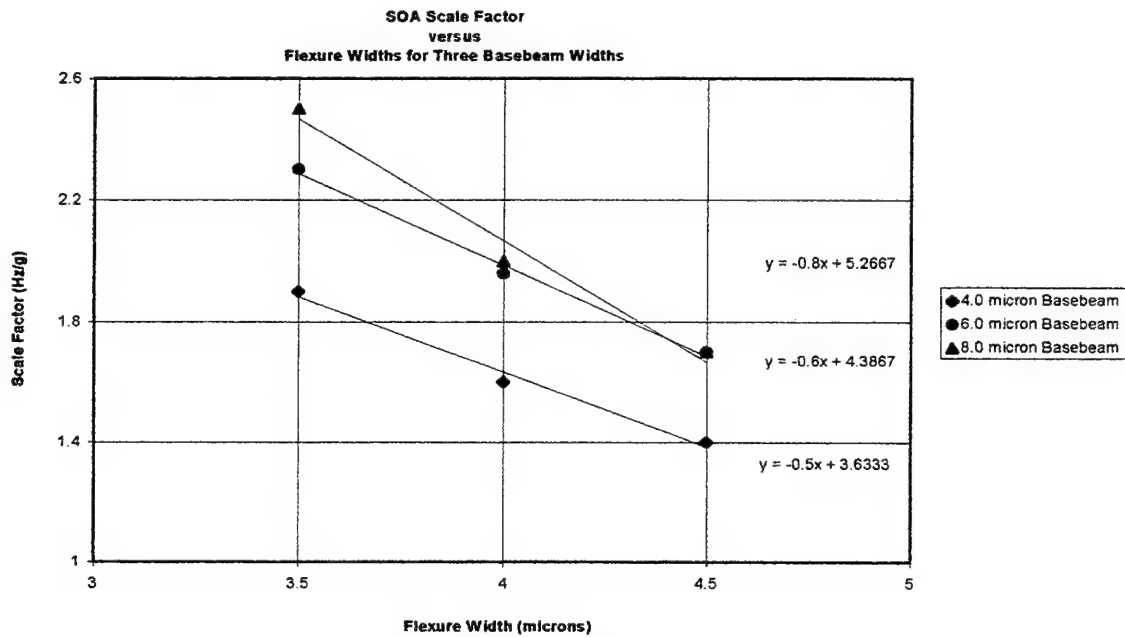


Figure 3.10: SOA FEA Scale Factor versus Flexure Width

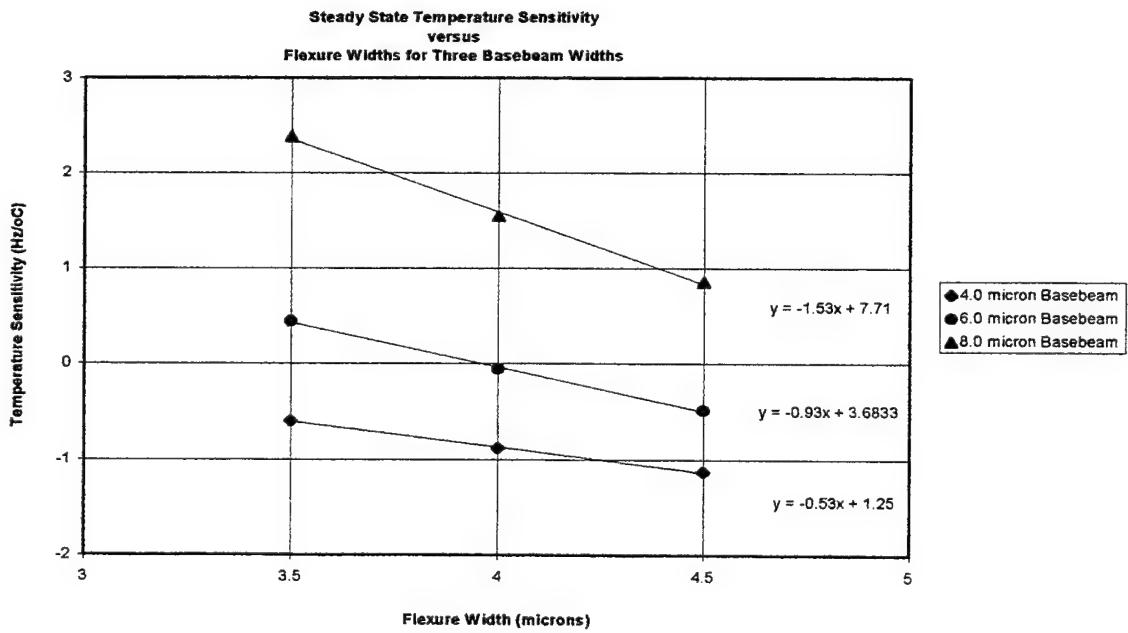


Figure 3.11: SOA FEA Temperature Sensitivity versus Flexure Width

ppm/°C. This graph shows that the six micron base beam and four micron flexure width device has been designed to nearly zero change in frequency per degree Celsius.

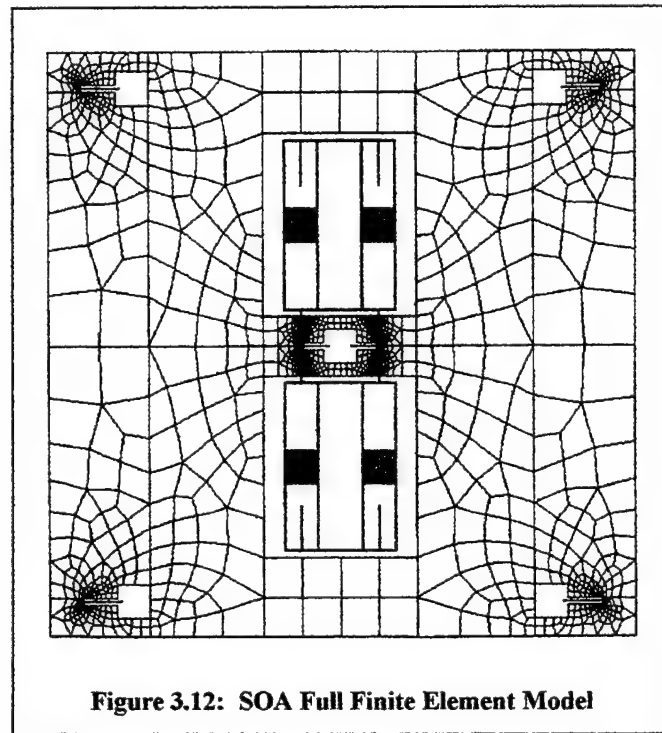
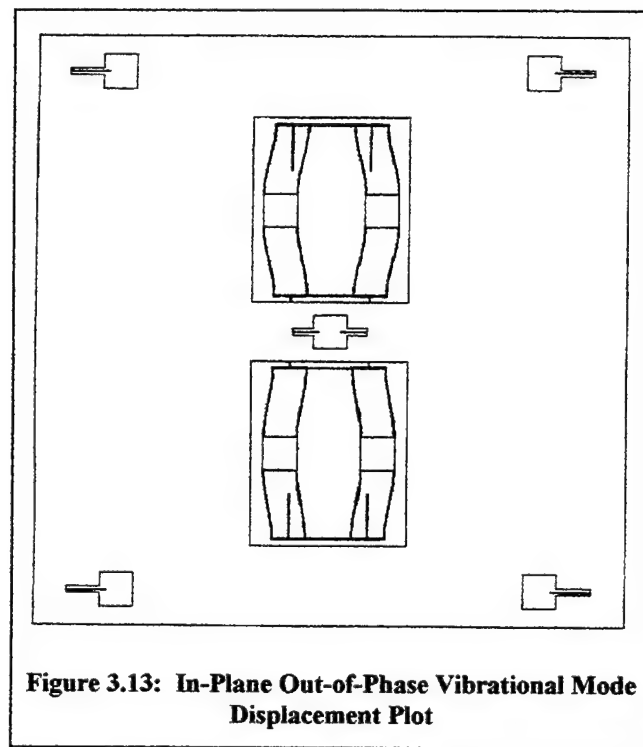


Figure 3.12: SOA Full Finite Element Model

Finite element analysis results for the out-of-plane element, full SOA model

The second stage of the detailed design was to determine the frequencies of out-of-plane plate bending vibratory modes. A full SOA finite element model was developed to accomplish this analysis. The ANSYS Shell93, eight node, structural shell elements were used with a specified twelve micron thickness and is described in the ANSYS User's Manual [24]. The finite element mesh was created by reflecting the quarter model area about the y-axis and then reflecting again about the x-axis. The elements and nodes were also reflected and duplicates eliminated. This full model, shown in

figure 3.12, contained 4,792 shell elements with 15,906 nodes. A modal analysis was then performed to find all, both the out-of-plane vibrational modes as well as in-plane, vibrational modes. The full SOA model, in-plane, out-of-phase oscillation mode of the resonators is seen in figure 3.13 as a scaled displacement plot.



The frequency of this mode was found to be 25,074.0 hertz using the out-of-plane elements as compared to 25,075.2 hertz presented in table 3.2 using the in-plane element formulation. The frequency of the in-phase oscillation mode was found to be 21,563.2 hertz using the out-of-plane elements versus the table 3.2 value of 21,564.6 hertz for the in-plane elements. Both modes were shown to be determined to within 0.01 percent difference of each other using the two different finite element formulations.

The out-of-plane mode results of these analyses are shown in figures 3.14a through 3.14h. These plots show the mode shape by displaying labeled displacement contours where displacement has been normalized to one. The lowest out-of-plane natural frequency was found to be 10.4 kHz, as shown in figure 3.14a, which is well above the required minimum of 2.0 kHz. No out-of-plane modes were within ten percent of the operating, out-of-phase, oscillating frequency, which is a key performance criteria. This was not the case on early analysis runs before revisions were made to "place" modes away from the drive frequency. By adjusting the anchor beam stiffnesses and their locations, out-of-plane modes that were within ten percent of the operating frequency of the oscillators were "placed" at greater than ten percent away. The 32.3 kHz mode shape, shown in figure 3.14h, for example, was originally at 25 kHz, the predicted operating frequency. In order to change this mode frequency to a value at least ten percent away from the operating frequency, the seismic mass anchors located in the center of the structure were shortened in order to reduce flexibility of the plate out-of-plane. This increased out-of-plane stiffness 'pushed' this mode frequency up to 32.3 kHz as shown in figure 3.14h.

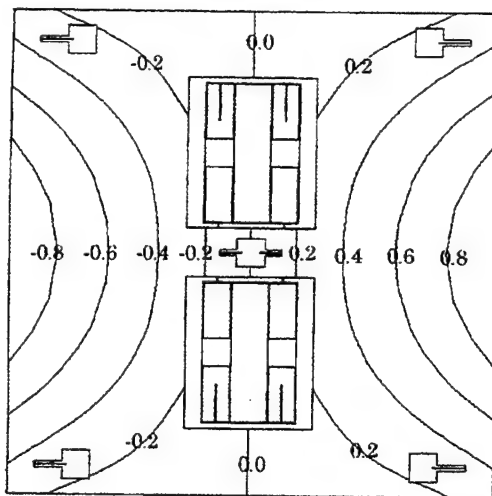


Figure 3.14a: SOA Out-of-Plane Vibrational Mode shown as normalized displacement contours; 10.4 kHz

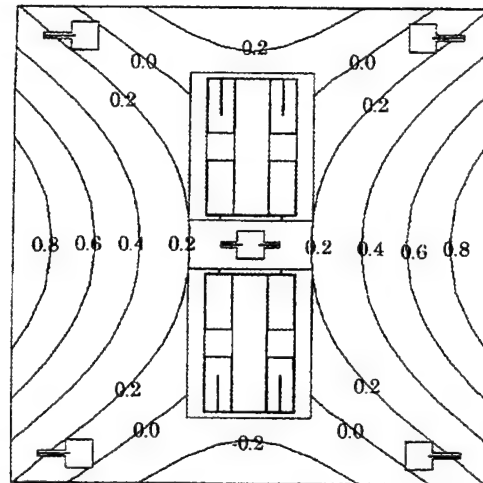


Figure 3.14b: SOA Out-of-Plane Vibrational Mode shown as normalized displacement contours; 10.6 kHz

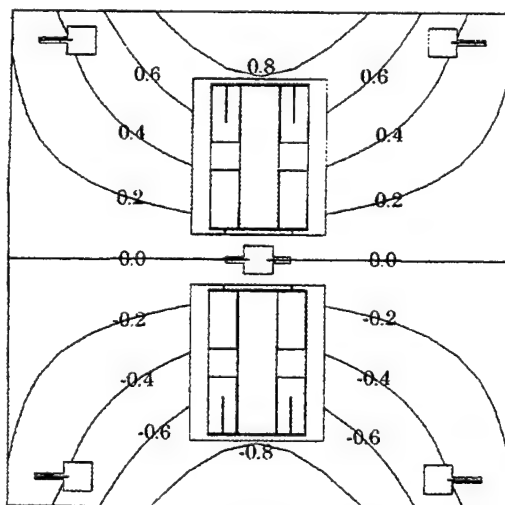


Figure 3.14c: SOA Out-of-Plane Vibrational Mode shown as normalized displacement contours; 12.3 kHz

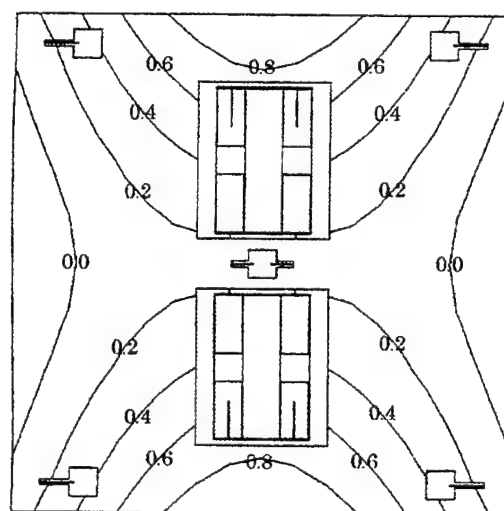
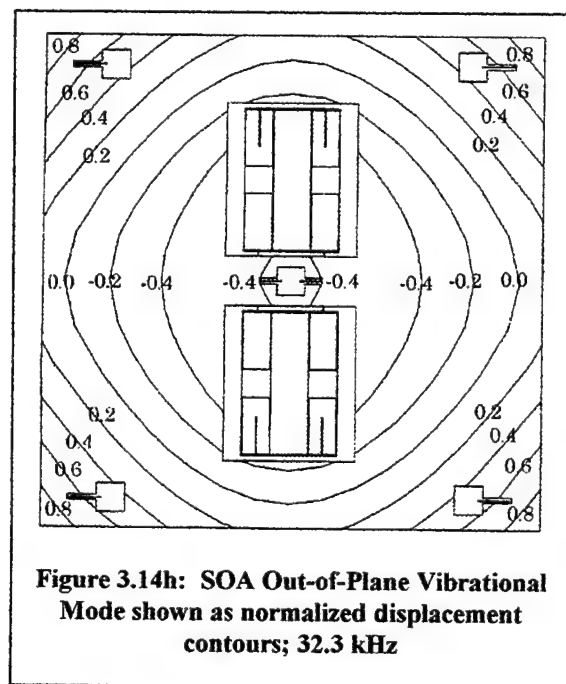
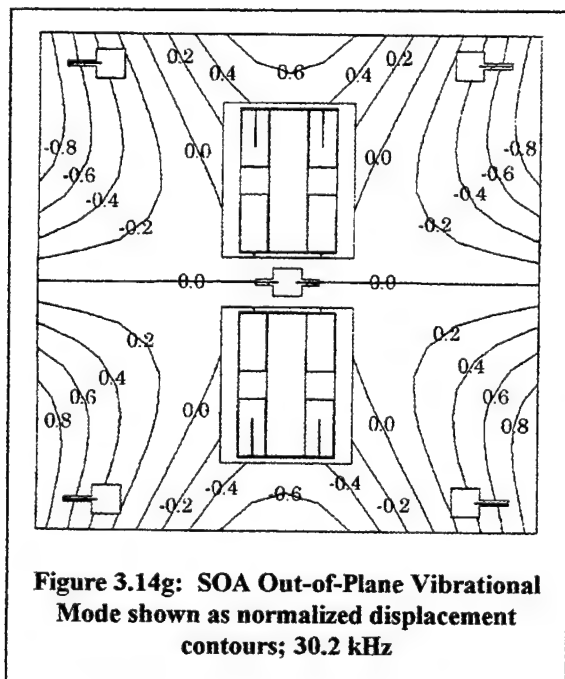
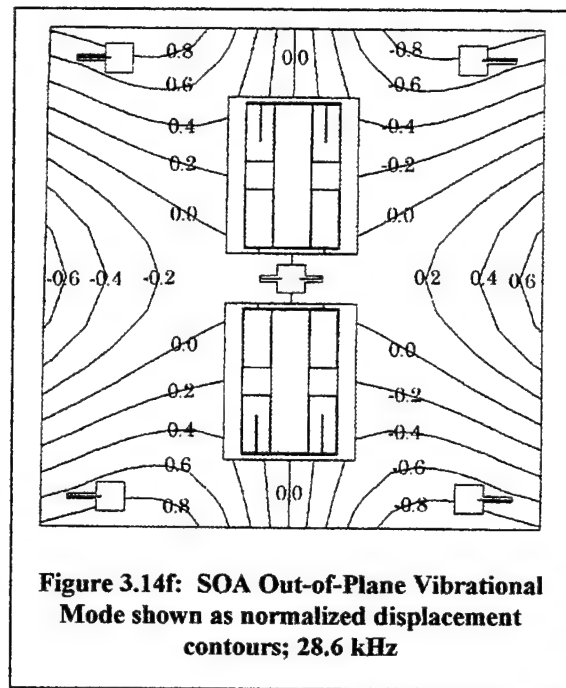
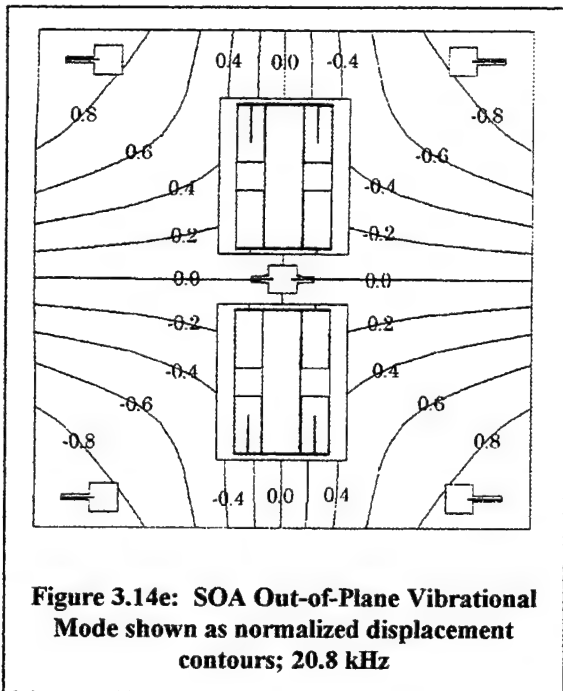
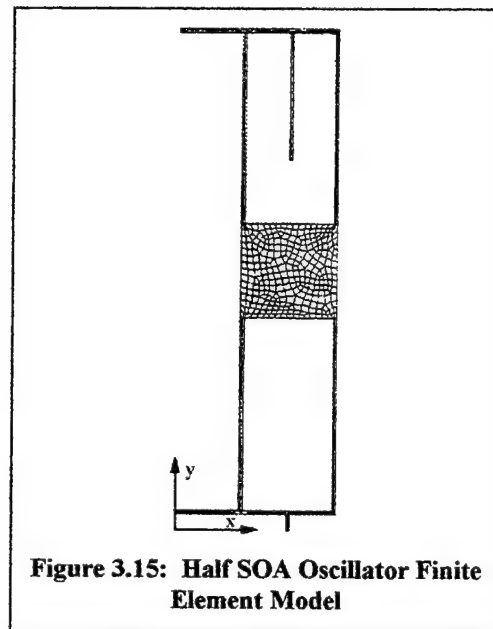


Figure 3.14d: SOA Out-of-Plane Vibrational Mode shown as normalized displacement contours; 13.3 kHz



Stiffness nonlinearity effect determination

In order to determine the effects of the vibrating beam stiffness nonlinearity on bias stability, (2.24) was used from the theory of operation section of this paper. This requires knowledge of the stiffness nonlinearity; specifically the coefficient on the term linear in displacement, α_1 , and the coefficient on the term cubic in displacement, α_3 . In order to determine these coefficients a finite element model of the oscillator was



developed. A half model of the oscillator was constructed as shown in figure 3.15. The anchor points of the oscillator were fixed to zero displacement, and a symmetry boundary condition was applied along the y-axis. A series of loads were applied to the mass in the x direction. For each of these loads, a nonlinear geometry static analysis was used to determine the mass displacement under that load. Figure 3.16 shows the stiffness

characteristic developed from this data.

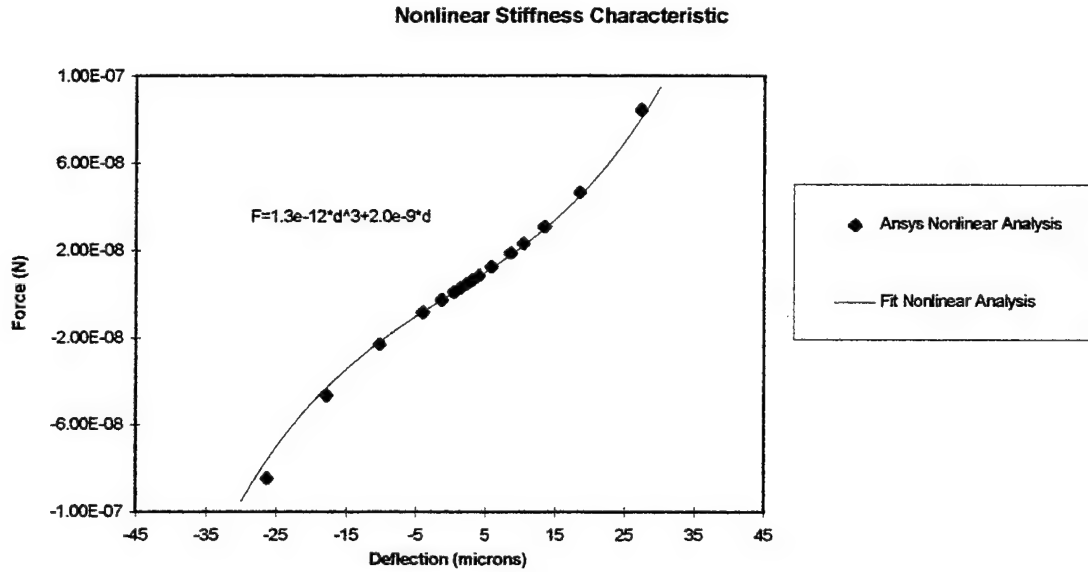


Figure 3.16: Oscillator Nonlinear Stiffness Characteristic

From this curve, the values of α_1 and α_3 were taken to be 2.0×10^{-9} newtons per micron and 1.3×10^{-12} newtons per micron cubed, respectively. These values, along with the assumptions that amplitude can be controlled to one hundred parts per million and that one micron will be the operating displacement amplitude of the oscillator, allow for calculating the bias stability of the instrument due to nonlinearity in vibrating beam stiffness. Substitution of these values along with a nominal operating frequency of 25 kHz, into (2.24), is shown to produce a change in frequency of 0.0013 Hz.

$$\begin{aligned} \Delta\omega &= 2 \left(\frac{3}{8} \right) \left(\frac{\alpha_3}{\alpha_1} \right) (x_o^2) \omega_o \left(\frac{\Delta x}{x_o} \right) \\ &= 2 \left(\frac{3}{8} \right) \left(\frac{1.3e^{-12}}{2.0e^{-9}} \right) (1)^2 (2.5e4) (10^{-4}) \end{aligned}$$

$$\Delta\omega = 0.0013 \text{ Hz}$$

Assuming a common mode rejection factor of ten and an instrument scale factor of four hertz per g gives a calculated bias stability of thirty three micro-g's due to vibrating beam stiffness nonlinearity. Smaller amplitude of oscillation would produce smaller calculated bias stability but also smaller output voltage signal from the sense capacitance preamplifier. In order to keep the signal to noise ratio sufficiently high, the one micron amplitude was selected.

Displacement under acceleration determination

To ensure that the SOA drive and sense electrostatic comb teeth do not bind during operation under acceleration, a maximum displacement was calculated using finite element analysis. An acceleration load of one hundred g's was applied to the SOA quarter finite element model and a static analysis performed. The results in table 3.3 show that one hundred g's along the z-axis produced the largest displacement. This displacement was approximately 0.3 microns. Since the drive and sense comb teeth are

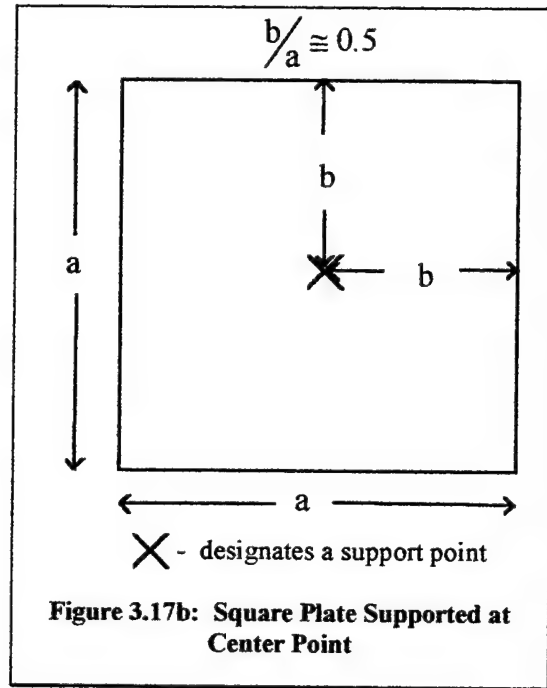
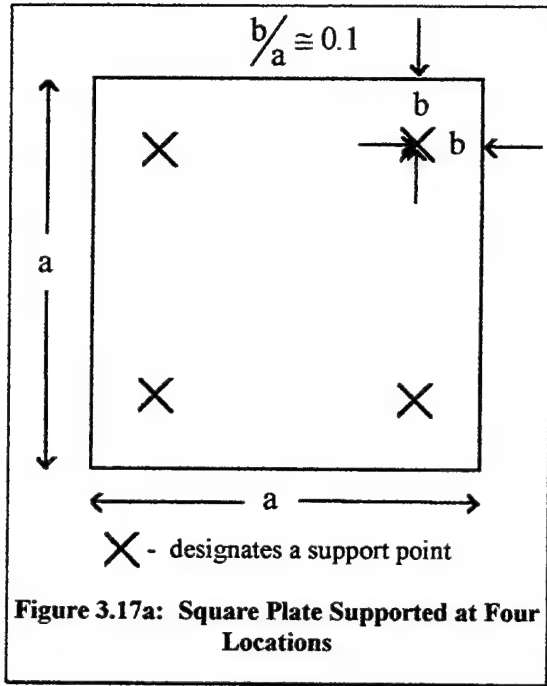
100 g loading direction	Maximum displacement
x-axis	0.04 microns
y-axis	0.08 microns
z-axis	0.28 microns

**Table 3.3: SOA Maximum Displacement for 100 g
Loading in the Primary Directions**

separated by two micron gaps, the comb teeth will not bind when the instrument is subjected to this one hundred g loading.

Verification of an out of plane mode

In order to independently verify the out-of-plane analysis results, an equation for



natural frequencies of a point-supported, square plate from Blevins was used [25]. The natural frequencies of the plate in bending, position constrained at four locations, shown in figure 3.17a, are

$$f_i = \frac{\lambda_i^2}{2\pi a^2} \left[\frac{Eh^3}{12\gamma(1-\nu^2)} \right]^{1/2}; i = 1, 2, 3, \dots \quad (3.2)$$

where f_i = the natural frequency,

E = Young's modulus,

ν = Poisson's ratio,

γ = mass per unit area of the plate,

a = length of side of square plate,

h = thickness, and

λ_i^2 = values shown in table 3.4 for a given 'b/a',

where b = the distance of the support from the plate edge.

The first three natural frequencies of a square plate point supported at four points were calculated using (3.2) and 'b/a' of 0.1 and 'a' of 2,630 microns. The results are shown in table 3.4. The first three natural frequencies of a square plate point supported at the center, as shown in figure 3.17b, were calculated using 'b/a' of 0.5 and shown in table 3.4.

The lowest common frequency between the two support configurations examined is shown as 13.9 kHz. From the out-of-plane finite element modal analysis, one of the natural frequencies of the SOA is consistent with minimal displacement at the plate four corner support locations and the plate center. This mode is shown in figure 3.14d and is at a frequency of 13.3 kHz. Since this mode could be independently verified to within five percent, the consistency of these separate analysis results builds confidence in the results.

b/a=0.1	Natural Frequency	b/a=0.5	Natural Frequency
$\lambda_1^2=12.89$	9,122 Hz	$\lambda_1^2=11.34$	8,026 Hz
$\lambda_2^2=19.69$	13,935 Hz	$\lambda_2^2=13.47$	9,533 Hz
$\lambda_3^2=23.97$	16,978 Hz	$\lambda_3^2=19.69$	13,935 Hz

**Table 3.4: Square Plate Natural Frequencies for Four Supports
and One Center Support**

4.0 EXPERIMENTAL PROCEDURE

4.1 Microfabrication of the SOA

The SOA design was drawn in Cadence, version 4.2.2, a commercially available computer aided design software package specialized for multi-layered integrated circuit design and drawing. Fillets, not modeled in the analysis, were applied to all inside corners in order to avoid stress concentrations. The required electronic files were sent to an external vendor for photolithography mask set manufacturing. These photomasks were used in fabricating the SOA.

The SOA was fabricated at Draper Laboratory using the silicon-on-glass bulk dissolved wafer process described in the background information section of this paper and shown in figure 2.6. Figure 4.1 is a photograph of the complete SOA chip on a penny to show scale.

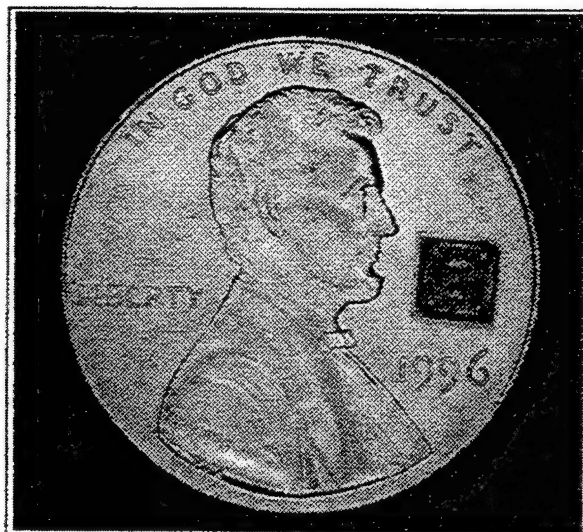
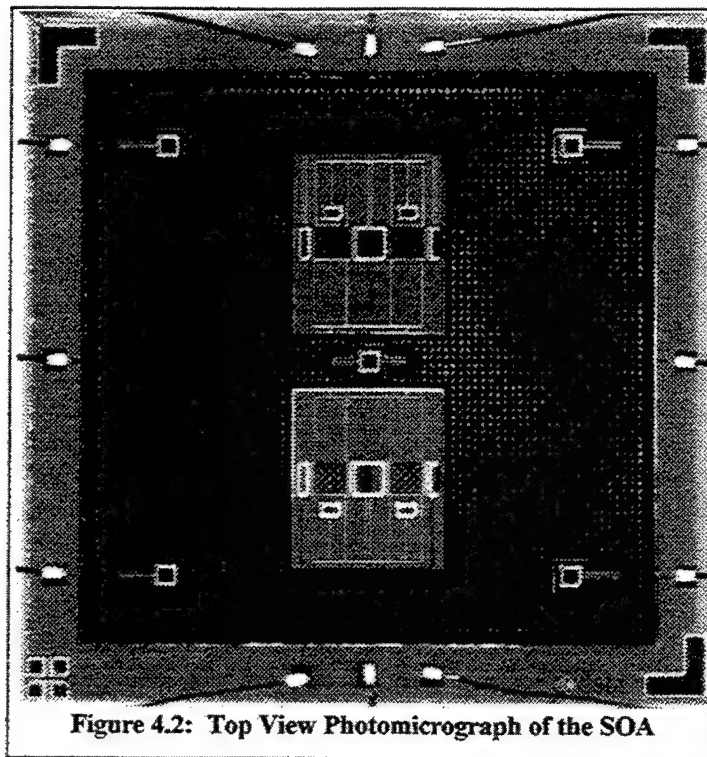


Figure 4.1: Microfabricated SOA Chip on a Penny to Show Scale

The micrograph in figure 4.2 was taken at 30 times magnification. Bond wires are shown



on each of the electrical bond pads.

A scanning electron microscope (SEM) was used to view details of the microfabricated SOA. The SEM is a destructive test since the object to be viewed is bonded to a pedestal and sputter coated with a thin layer of gold. A scanning electron micrograph of the SOA oscillator flexure and oscillator mass is shown in figure 4.3. Figure 4.4 is an SEM image showing the engaged electrostatic comb teeth of an SOA oscillator. The structure thickness in both figure 4.3 and figure 4.4 is twelve microns, showing the scale. Data from the SEM showed that the initial SOA oscillator flexure widths were, on average, three tenths of a micron larger than designed. This oversize can be corrected during fabrication of future devices but test data contained here is for

devices of this slightly wider flexure width. We take account of this greater flexure width in subsequent sections.



Figure 4.3: SEM of SOA 12 Micron Thick Oscillator Mass and Flexure

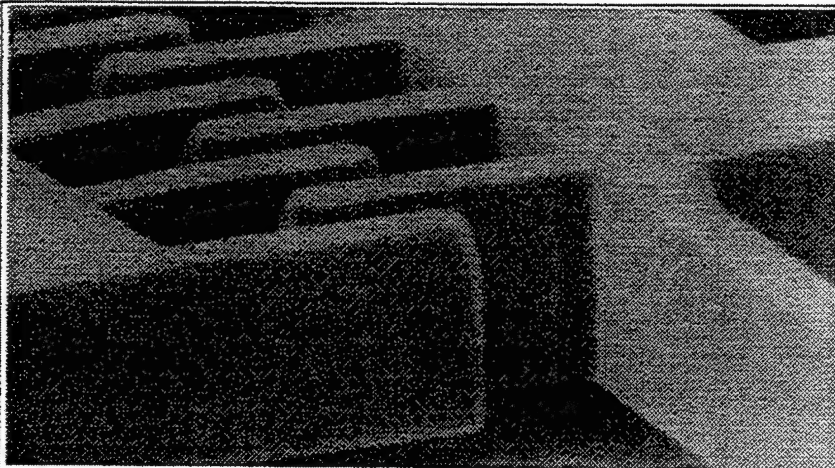
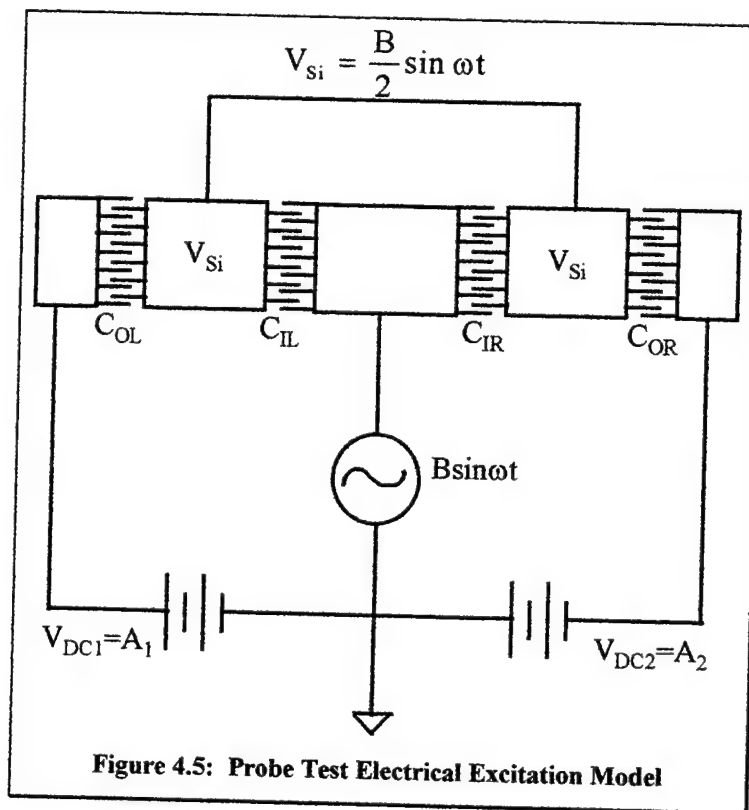


Figure 4.4: SEM of SOA 12 Micron Thick Electrostatic Comb Teeth

4.2 Preliminary testing

The first phase in assessing viability of the newly fabricated SOAs was to individually test the two SOA oscillators in air at a probe station. The probe station testing was accomplished before any steps to package the device in a vacuum enclosure were taken. A Wentworth Laboratories magnetic probe station in conjunction with a Bausch & Lomb high performance microscope magnifying at two hundred and fifty times were used for probe testing. A General Radio Strobotac strobe light was aligned with the input light port of the microscope to provide a frequency adjustable light source for



viewing the vibrational mode being excited.

The electrical model [26] presented in figure 4.5 shows the silicon oscillator vibrating mass potential as V_{si} . This potential is developed due to a voltage division of

the sinusoidal signal, $B \sin \omega t$, across the inner and outer comb teeth capacitors of a single silicon mass. These inner and outer comb teeth capacitors are of equal value when the silicon mass is centered. The two silicon masses were electrically floating and are shown electrically connected because they are physically joined by conductive boron-doped silicon flexures. Since the outer comb capacitor C_{OR} is approximately the same as C_{IR} when centered, the voltage divider gives

$$V_{Si} = B \sin \omega t \left(\frac{C_{OR}}{C_{IR} + C_{OR}} \right) \quad \text{or}$$

$$V_{Si} = \frac{B}{2} \sin \omega t. \quad (4.1)$$

With the steady voltage, $|A_2| > |B|$, applied as shown in figure 4.5, the voltage across the outer comb teeth capacitor is given by

$$V = A_2 + \frac{B}{2} \sin \omega t, \quad \text{or as in (2.11),}$$

$$V^2 = A_2^2 + \frac{\left(\frac{B}{2}\right)^2}{2} + \frac{\left(\frac{B}{2}\right)^2}{2} \cos 2\omega t + 2A_2B \sin \omega t.$$

Therefore the total electrostatic drive force is

$$F_{\text{total}} = n \frac{\epsilon w}{2g} \left[A_2^2 + \frac{\left(\frac{B}{2}\right)^2}{2} + \frac{\left(\frac{B}{2}\right)^2}{2} \cos 2\omega t + 2A_2B \sin \omega t \right].$$

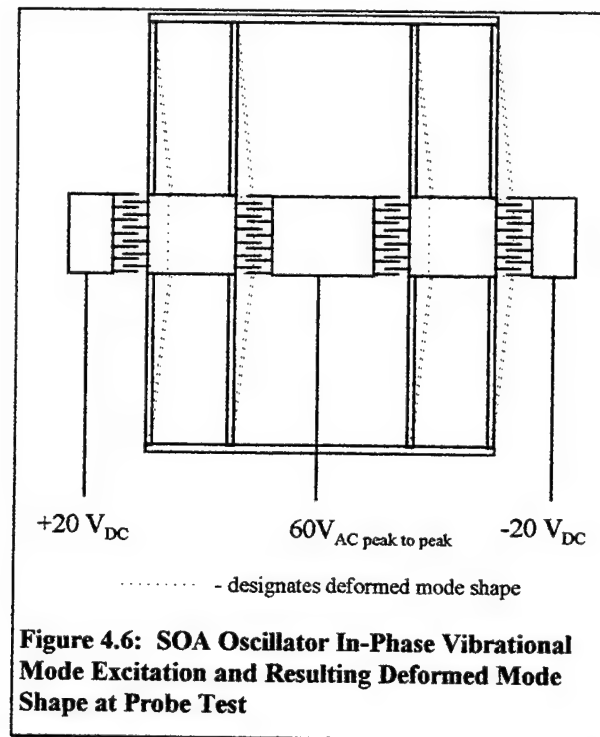
The insignificant drive terms which do not drive at the resonant frequency are the first two terms which are constants and the third term which drives as 2ω . Neglecting these insignificant drive terms, as in (2.15), gives

$$F_{\text{total}} = n \frac{\epsilon w}{g} [A_2 B \sin \omega t]. \quad (4.2)$$

This shows the total attractive force exerted on the silicon mass contributing to the resonant oscillation due to the outer comb teeth capacitor. Since this force is at the frequency of the electrical excitation, by varying the frequency of excitation and noting the frequency that causes the oscillator to resonant, the structure resonant frequency is determined. The steady bias signals applied to the outer comb teeth determined which mode, in-phase or out-of-phase oscillation, was excited. If $A_1=A_2$ then the outer capacitors cause an in-phase attraction of the masses which caused the two oscillator masses to move out-of-phase. This out-of-phase motion is the operating, or “tuning fork” mode. If $A_1=-A_2$ then the outer capacitors cause an out-of-phase attraction of the masses which causes the oscillator masses to move in-phase.

SOAs fabricated with a 3.5 and 4.0 micron flexure width were used to determine the in-phase vibrational mode frequency. The in-phase oscillation mode of the oscillator was excited using the electrical input configuration shown in figure 4.6. Positive twenty volt direct current and a negative twenty volt direct current potentials were applied to the outer electrostatic comb teeth of one oscillator. A Hewlett-Packard Harrison 6205B dual DC power supply was used to produce these signals at the probes. The needle point probes used to make all electrical connections to the device, were lowered until they contacted the metalized electrical bond pads. A sixty volt peak-to-peak alternating current signal was applied to the center electrostatic comb teeth. This alternating current signal was produced by a Hewlett-Packard 3325A Synthesizer/Function Generator and monitored with a Tektronix 2465 Oscilloscope. The variable frequency of the alternating

current signal was adjusted to produce an approximated maximum amplitude of oscillation as observed visually under magnification. The approximate maximum occurred at or near 19,595 Hz. The in-phase vibrational mode was confirmed by



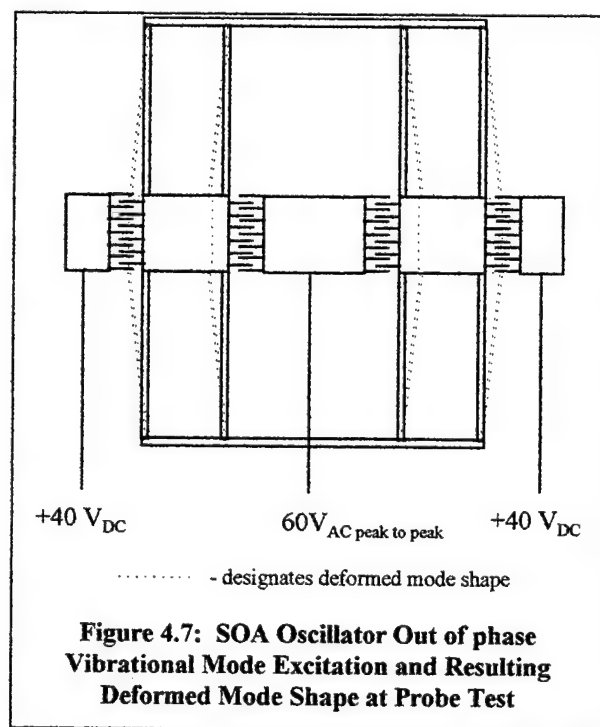
adjusting the strobe frequency until the mode displacement could be observed visually.

When the strobe is adjusted properly, the in-phase motion of the oscillator masses becomes quite obvious.

The out-of-phase, "tuning fork," vibrational mode of the oscillator was excited using the electrical input configuration shown in figure 4.7. Units fabricated to have a 3.5, 4.0, and 4.5 micron flexure widths were used during viability tests and to determine the out-of-phase vibrational mode frequency. A positive forty volt bias potential was applied to the outer electrostatic comb teeth using the same power supply as for exciting

the in-phase mode. Again a variable frequency sixty volt peak-to-peak alternating current potential was applied to the center electrostatic teeth from the function generator. The frequency of this alternating current signal was varied until approximate maximum amplitude was visually observed. This maximum occurred at 23,670 Hz and was the operating frequency of this 3.5 micron flexure width device. Again the strobe light was used with the microscope to verify that the out-of-phase oscillation mode was being observed.

After the in-phase mode was confirmed to be at least 10% lower than the out of



phase mode for two of the units, the 3.5 and the 4.0 micron flexure widths, this in-phase mode test was no longer run. The out-of-phase mode was the mode of interest. Table 4.1 lists the results of the probe tests in air for several SOAs.

SOA Designed Flexure Width (microns)	Out-of-Phase Oscillation Frequency (kHz)	In-Phase Oscillation Frequency (kHz)
3.5	23.7	19.6
3.5	24.1	
3.5	23.8	
4.0	27.7	24.2
4.0	28.0	
4.0	28.1	
4.5	32.6	
4.5	32.4	
4.5	32.9	

Table 4.1: SOA Probe Test Results for Out-of-Phase and In-Phase Oscillation Frequency

Figure 4.8 is a graph of predicted and experimentally determined SOA out-of-phase resonant frequency versus vibrating flexure width for several SOAs. A correction was made to the flexure width to account for SEM data showing larger flexures as presented in section 4.1 of this paper. This graph shows that the predicted values are within 5% of the experimental values for the out-of-phase vibrational frequency. Similarly, figure 4.9 is a graph of the predicted and experimentally determined SOA in-phase resonant frequency versus oscillator flexure width for two SOAs. This graph shows that the predicted values for the in-phase oscillation frequency are within 5% of the experimental values.

SOA Antiphase Resonant Frequency

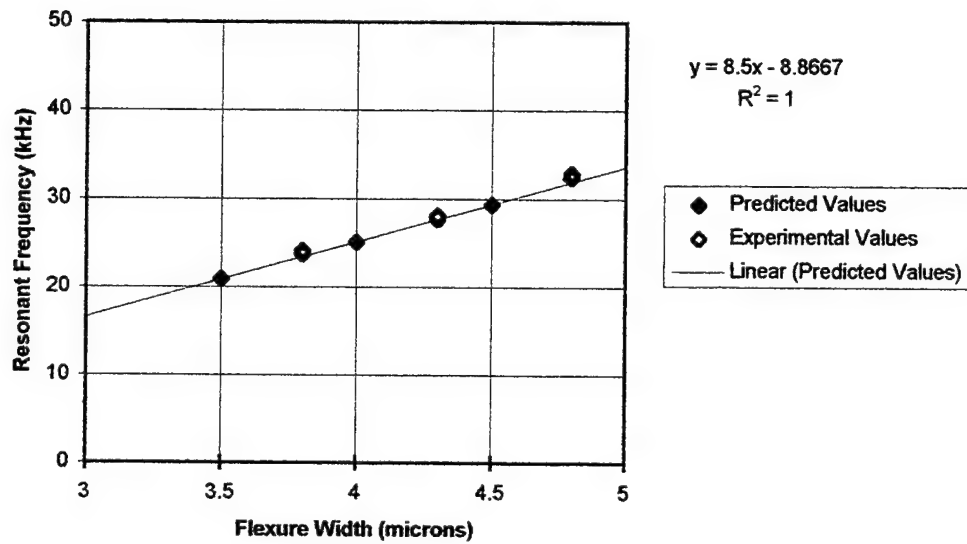


Figure 4.8: Analytical and Experimental SOA Out-of-Phase Oscillation Resonant Frequency versus Flexure Width

SOA Inphase Resonant Frequency

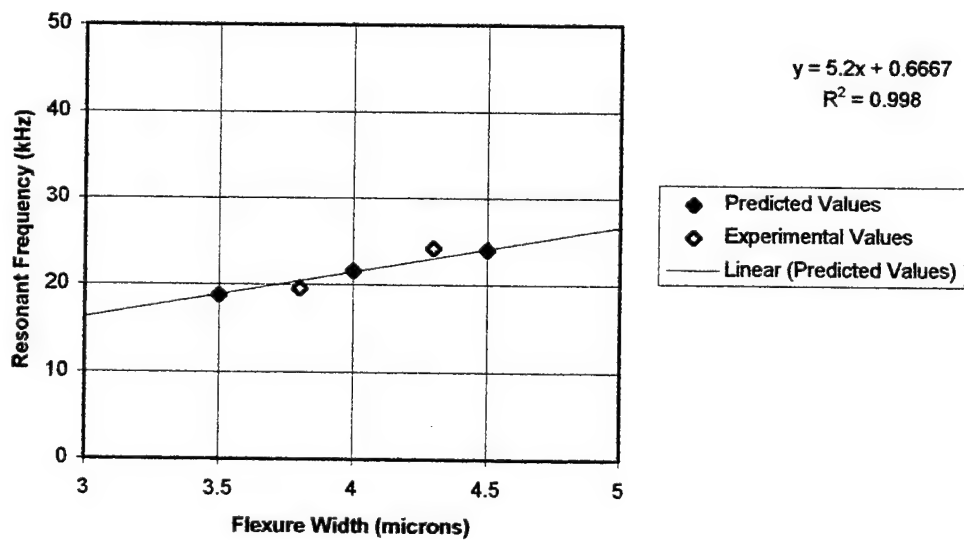
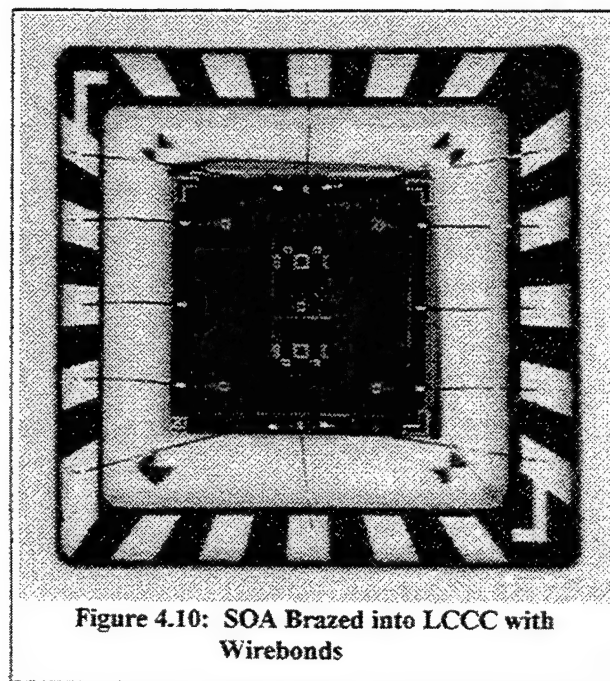


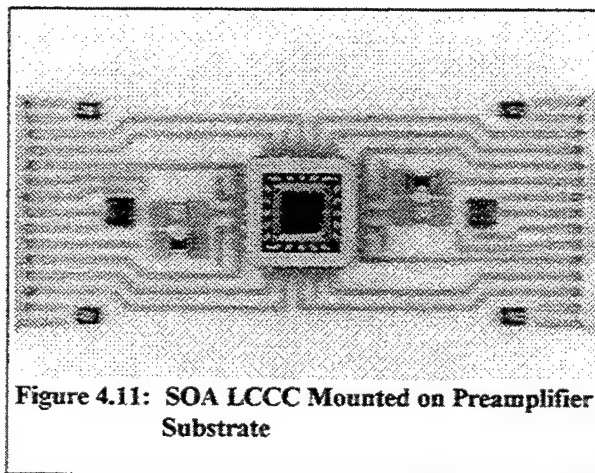
Figure 4.9: Analytical and Experimental SOA In-Phase Oscillation Resonant Frequency versus Flexure Width

4.3 Packaging and electronics

After probe testing, the SOAs with satisfactory performance were packaged and integrated with preamplifier electronics. Satisfactory performance meant clean units with all bonds, flexures, and electrostatic comb teeth visually intact as well as both oscillators resonating as expected while observed visually under magnification. Packaging involved brazing the SOA chip with a metalized bottom surface of the glass into a leadless ceramic chip carrier (LCCC). A braze pre-form, cut to the appropriate size, was clamped between the chip and the LCCC and heated to the brazing temperature to accomplish the bond. The appropriate wire bonds for electrical connection between the SOA bond pads and the appropriate internal chip carrier pins were then made. These wire bonds were accomplished using 0.001 inch, 99% aluminum, 1% silicon wire and a Mech-El Industries ultrasonic wire bonder. The SOA chip in an LCCC, after brazing and wire bonding, is shown in figure 4.10.



Before the LCCC containing the accelerometer is sealed, qualification tests are run to determine the viability of the unit's oscillators. To perform these tests the LCCC could either be bonded directly to an alumina substrate with conductive epoxy, as shown in figure 4.11, or placed into a "fuzz-button" connector that in turn is bonded to the alumina substrate. The advantage of the "fuzz-button" connector is the ease and speed at which LCCCs could be removed and replaced onto the substrate. The preamplifier electronics discussed in the theory of operation section, section 2.1 of this paper, are also mounted on the alumina substrate. Four temperature sensors are located near the four corners of the substrate and a series of pins protruding from both sides of the alumina allow for clamping the substrate into the test station while making the necessary electrical contact.



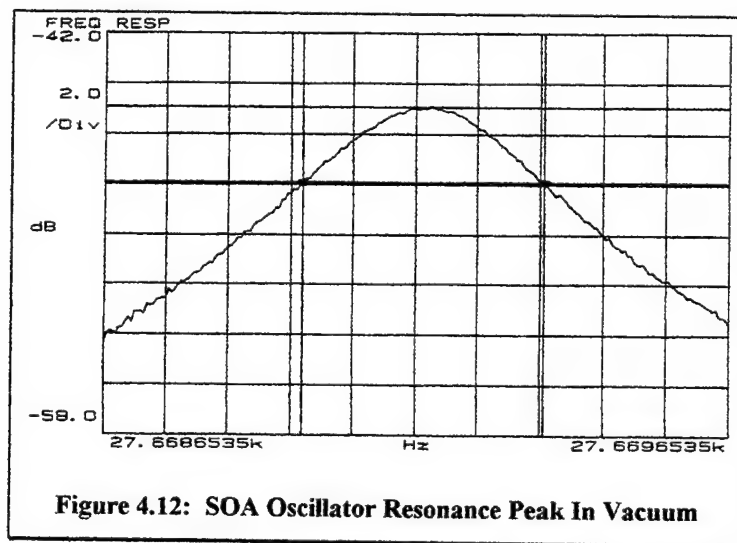
After assessing the oscillator viability the LCCC was sealed by brazing in vacuum a metallic cover onto the LCCC. Pressures less than one millitorr were achieved contributing directly to high Q factors.

4.4 SOA testing and results

Upon sealing the LCCC, the accelerometers were ready for testing. The vacuum enclosed unit with the preamplifier electronics was clamped into a test fixture which also housed the individual automatic gain control (AGC) circuitry for each oscillator. This set of electronics used feedback to sustain the oscillators in a state of resonance even when the resonant frequency was changing.

Quality factor data

A Q test or quality factor test was performed first. The device was run open loop by bypassing the AGC circuit and applying a controlled frequency, sinusoidal input to the electrostatic drive comb teeth. A Hewlett-Packard 3563A Signal Analyzer was used to produce the input as well as to monitor the output from the SOA preamplifier. Plotting



the output-to-input ratio versus the frequency shows a peak in response at the resonant frequency of the oscillator. An example of the resonant peak is shown in figure 4.12. A

Q factor was calculated from this open loop response to be approximately one hundred twenty thousand. The Q factor is defined here as

$$Q = \frac{\omega_o}{\Delta\omega|_{-3 \text{ dB from peak}}}$$

The results of running the same Q test on the other oscillator of the same instrument independently, were essentially the same. Other sealed SOA units have exhibited Q factors as high as two hundred fifty thousand.

The same Q test was performed on another SOA before sealing. This test was done to compare the Q value with no vacuum, in air, to the quality factor measured earlier in vacuum. The calculated Q factor from this test was two hundred; six hundred times lower than the vacuum-sealed unit.

Acceleration sensitivity data

A one g inversion test was performed to determine the scale factor of the SOA. The scale factor is the sensitivity of the instrument in hertz per g to acceleration along the input axis of the device. The test was performed by first allowing the instrument frequency output from the oscillators to stabilize before recording data. After stabilizing, the frequency output from both oscillators was acquired using Labview, a commercially available software, to record the oscillator frequency every 1.8 seconds. Several minutes of data were acquired with the accelerometer oriented with the input axis parallel to the ground. After this baseline data was recorded, the accelerometer was turned so that the input axis of the device was perpendicular to the ground. This effectively places the seismic accelerometer mass in the gravitational acceleration field of the Earth, 9.8 m/s^2

SOA ± 1 g Acceleration Inversion Test; Top Oscillator

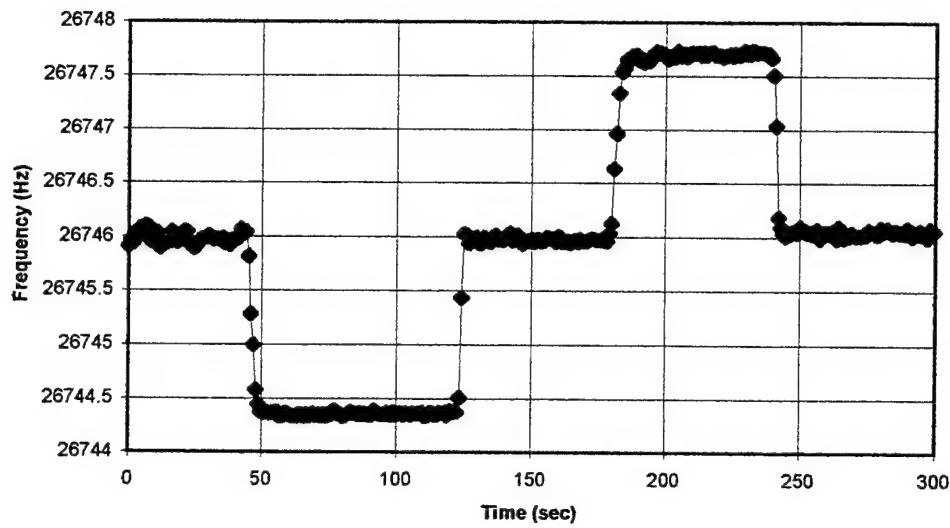


Figure 4.13a: SOA ± 1 g Inversion Test Top Oscillator Frequency Response

SOA ± 1 g Acceleration Inversion Test; Bottom Oscillator

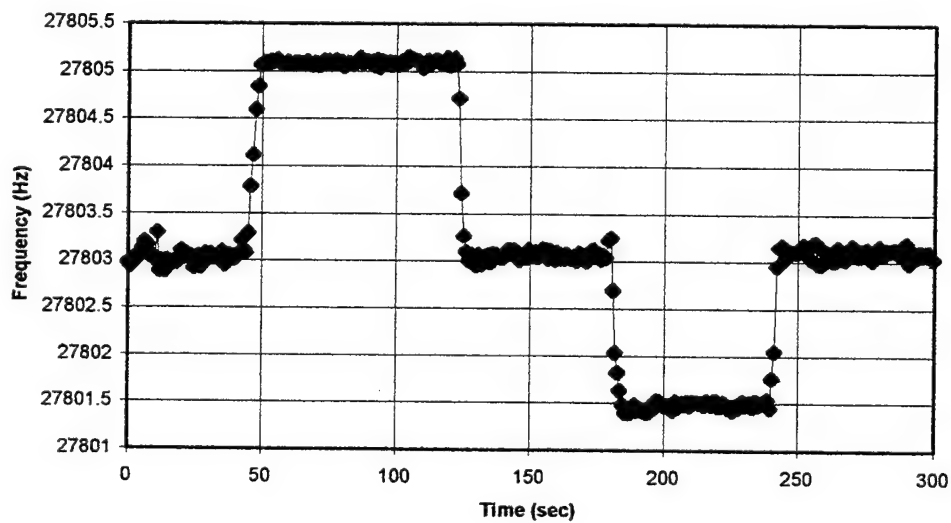


Figure 4.13b: SOA ± 1 g Inversion Test Bottom Oscillator Frequency Response

SOA ± 1 g Acceleration Inversion Test

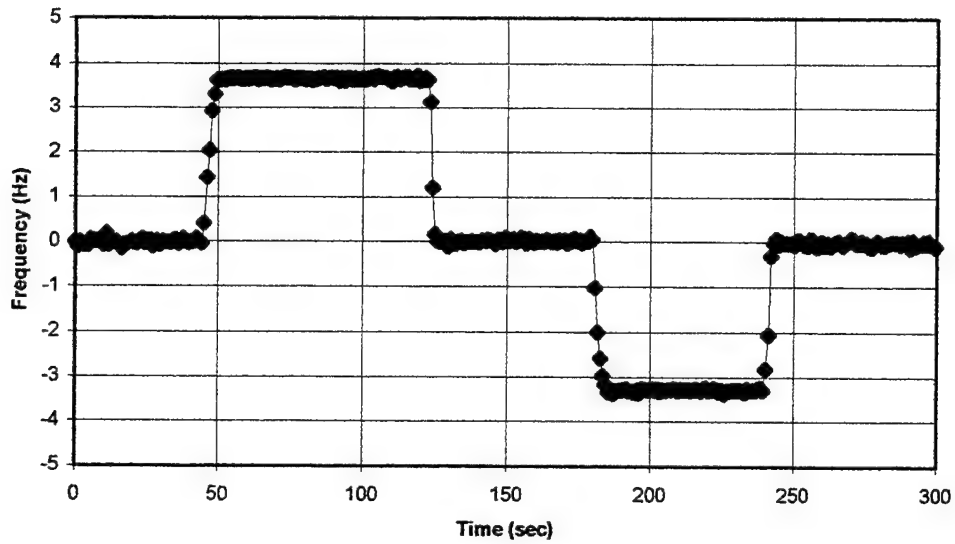


Figure 4.13c: SOA ± 1 g Inversion Test Total SOA Instrument Response

Second SOA ± 1 g Acceleration Inversion Test; Top Oscillator

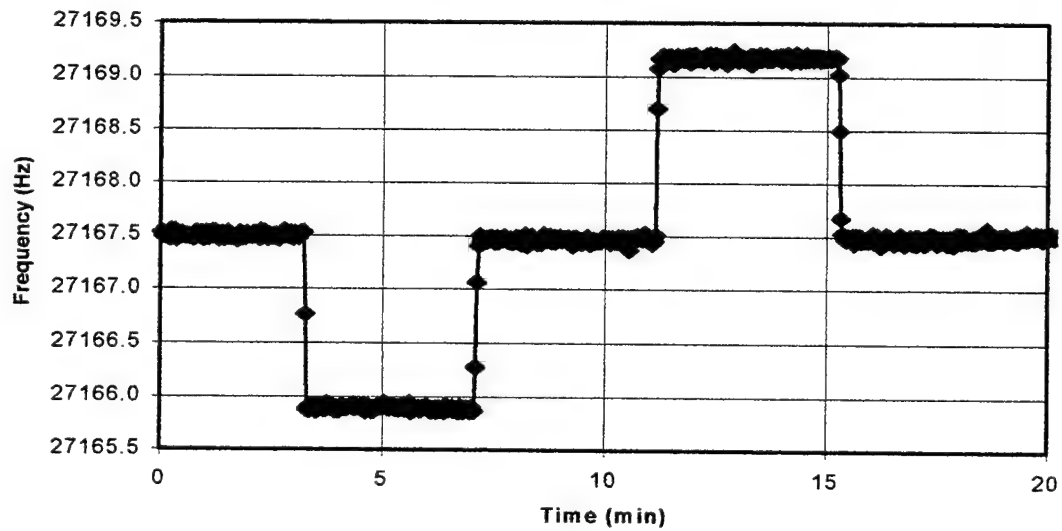


Figure 4.14a: SOA ± 1 g Inversion Test Top Oscillator Frequency Response

**Second SOA ± 1 g Acceleration Inversion Test; Bottom
Oscillator**

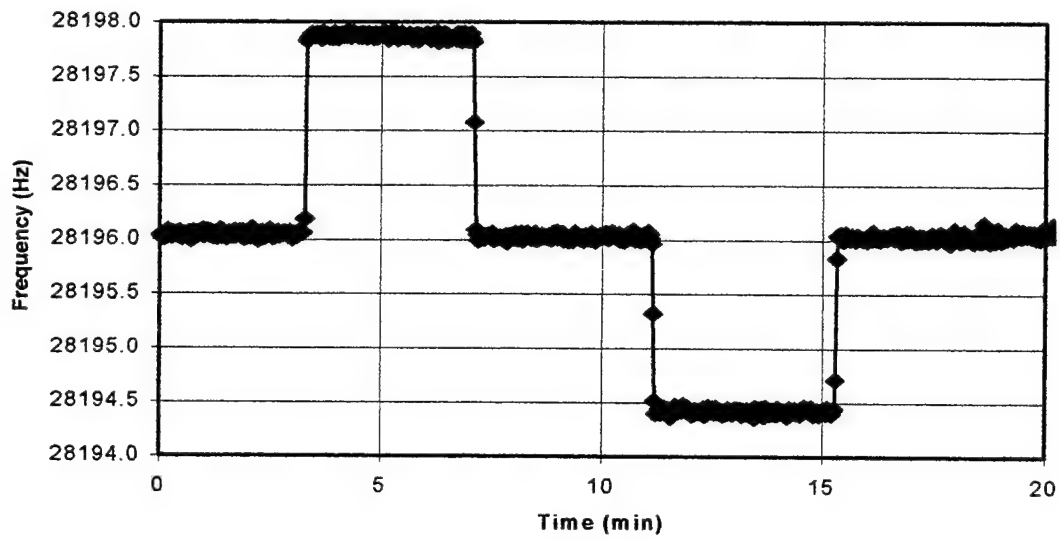


Figure 4.14b: Bottom Oscillator 2nd SOA ± 1 g inversion

Second SOA ± 1 g Acceleration Inversion Test

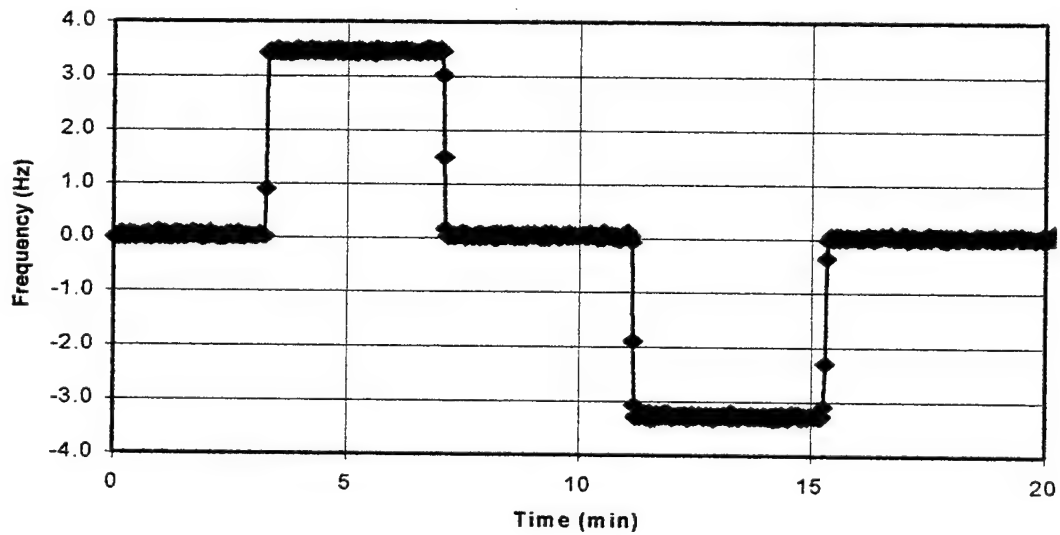


Figure 4.14c: Instrument response 2nd SOA ± 1 g inversion

or one g. This produced an expected shift in the resonant frequencies of the SOA's oscillators. The data for each oscillator is shown in figures 4.13a and 4.13b. The frequency output from the oscillators was differenced and adjusted to zero and the result presented in figure 4.13c as the total instrument response. This data in figure 4.13c shows that the SOA has a total frequency response to input axis acceleration of approximately 3.5 Hz/g. This experimental data point for acceleration sensitivity was then compared to the finite element method predicted value for instrument scale factor in figure 4.15. This figure shows that the SOA's experimentally determined scale factor is in good agreement with the predicted value to within ten percent.

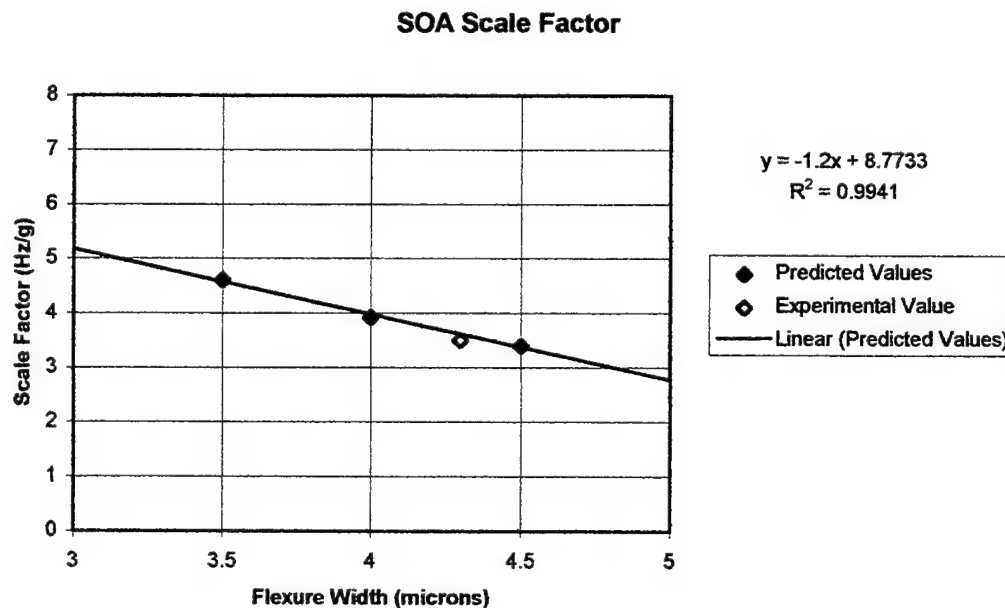


Figure 4.15: Analytical and Experimental SOA Scale Factor versus Flexure Width

An asymmetry of the frequency shift of the two oscillators to tension and compression exists for both units tested. This different gain in response to ± 1 g

acceleration is especially prevalent in the bottom oscillator of both units tested as shown in figures 4.13b and 4.14b. Figures 4.13c and 4.14c show that the sensitivity of the device, or differential frequency shift, to acceleration in one direction, +1 g, is greater than the sensitivity of the instrument to -1 g acceleration. Some possible explanations for this behavior include a poor or failed electrostatic bond of one or more silicon anchors or a particle wedged under the seismic mass that allows the mass to move more freely in one direction than the other. Since the largest asymmetry is associated with the bottom oscillator, there may also be some systematic asymmetry in the fabricated parts. This problem was not investigated further herein due to time limitations, but should be studied in future work.

Thermal sensitivity data

The sealed SOA, with associated electronics, was then placed in an oven to control temperature to at least a tenth of a degree Celsius. The instrument was operated at a nominal twenty five degrees Celsius in order to establish baseline temperature data. The temperature was then ramped up to forty five degrees Celsius to determine the shift in frequency experienced by the individual oscillators. Figure 4.16a shows the data acquired during this oven controlled temperature experiment. This figure shows the major frequency trend of the oscillator with numerous anomalous output spikes. The anomalous frequency output spikes are peculiarities that are not seen when the device is operated at room temperature. Some possible explanations for these spikes could be electronic interference from the surrounding oven enclosure, faulty electrical connections that are aggravated by thermal expansion, or adverse heating effects on the instrument

electronics. The data in figure 4.16b is the same data as shown in figure 4.16a with the anomalous frequency spikes removed. This figure shows an approximate eight hertz shift

SOA Oscillator Frequency with 20 °C Temperature Shift and Anomalous Spikes

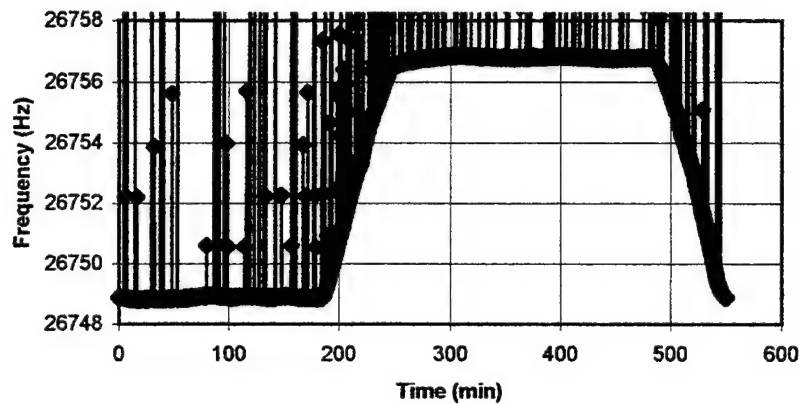


Figure 4.16a: SOA Oscillator Temperature Response

SOA Oscillator Frequency with 20 °C Temperature Shift in Oven

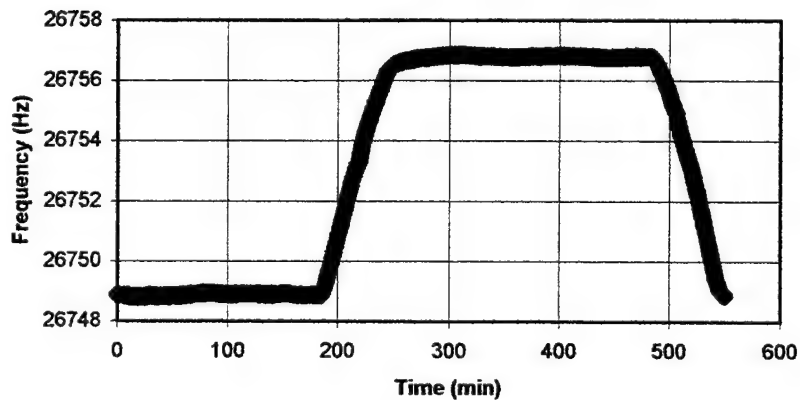


Figure 4.16b: SOA Oscillator Temperature Response

in oscillator frequency over the twenty degree Celsius temperature increase. The temperature sensitivity analysis performed as described in the theory of operation section of this paper, using $2.6 \times 10^{-6}/^{\circ}\text{C}$ as the thermal expansion coefficient of silicon and -52 ppm/ $^{\circ}\text{C}$ for the change in Young's modulus of silicon with temperature, produced a result of 0.38 hertz per degree Celsius frequency shift of the oscillator. This result agrees with the experimental data seen to-date to within ten percent.

5.0 CONCLUSIONS AND RECOMMENDATIONS

Testing of the SOA to-date has shown good agreement between analytical results and experimental results. This research effort has demonstrated that the concept, as planned and executed, works. The analysis models used to design the SOA are very accurate in predicting resonant frequency, 27 kHz, and instrument scale factor, 3.5 Hz/g, both values predicted to within ten percent. The oscillator temperature sensitivity, 0.4 Hz/°C, was also predicted to within ten percent. This data has been presented after testing only two packaged units; testing of more units is required.

More testing of the current devices after resolving the issues of oscillator tension/compression asymmetry and anomalous frequency spikes is required to determine long term stability under temperature control, actual common mode rejection observed, and device response to dynamic input accelerations.

Studying the vibrating flexure's preload due to the fabrication bonding process and the thermal expansion mismatch between silicon and Pyrex and this preload's effect on the nonlinearity characteristic of flexure stiffness could provide insight into the asymmetry of the oscillator's response to acceleration. Performing the one g inversion test with a steady, slow inversion rate as opposed to flipping the device quickly could help to determine how and when, during the inversion, the asymmetry occurs. The anomalous spikes in frequency are almost surely caused by an interaction of the instrument test electronics with the electrical environment. Electrical effects, such as the oven controller and heating element cycling, should be investigated through further testing as possible causes of this phenomenon.

Several recommendations for increased performance have come from analysis and test results. One recommendation for increased performance is to design an instrument with increased primary sensitivity. Increased primary sensitivity will increase the resolution of the instrument, making it possible to measure frequency changes associated with smaller input accelerations. One method to increase primary sensitivity would be to push the process technology in order to fabricate a thicker and larger surface area seismic mass. By increasing the thickness, not only is the seismic mass increasing thus causing more tension and compression load when accelerated but also extraneous out-of-plane plate bending vibrational modes would be pushed higher due to plate stiffening. Then by increasing surface area, the seismic mass again increases.

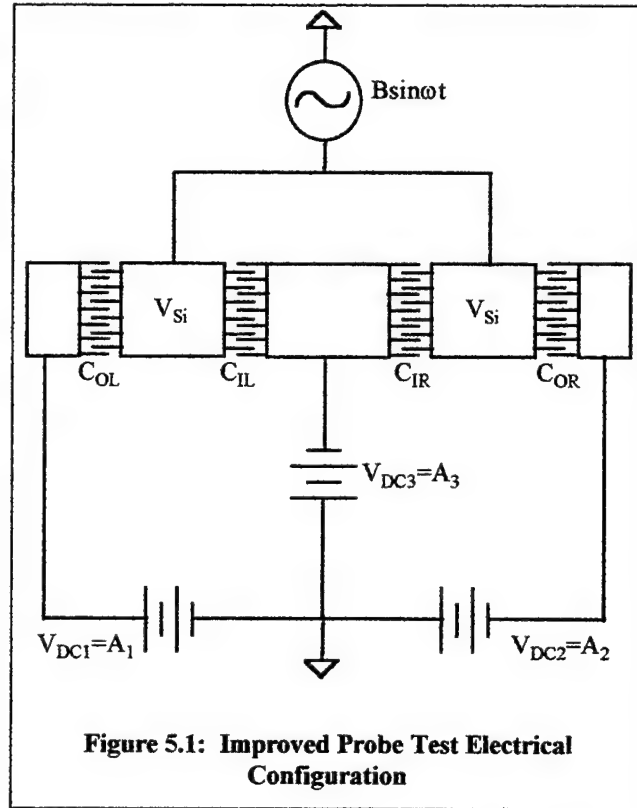
Temperature sensitivity should be reduced in future design revision since it has been shown that a model, using appropriate values for silicon's thermal expansion coefficient and the change of Young's modulus of silicon, exists that is capable of predicting the oscillator's thermal sensitivity.

During probe testing, residual particles from fabrication are suspected to be under the seismic mass, and have also been seen reducing yield of units with viable resonators by being permanently wedged under the oscillator masses. It follows that increasing the gap size between the glass and silicon could alleviate this condition. Again pushing the fabrication technology could increase device yield and could improve the response of the device.

Another recommendation is to change the electrical configuration for testing SOAs at the probe station [26]. A major improvement to the current probe test configuration for the SOA, shown in figure 4.5, would be to use the outer and inner comb

teeth capacitors to force oscillations of the masses instead of only the outer capacitors.

Also by exciting the proof masses with the varying sinusoidal signal, as shown in figure



5.1, the electrostatic force per capacitor is doubled because the voltage divider from the current test setup would be eliminated. For the recommended electrical configuration shown in figure 5.1, $V_{DC1}=V_{DC2}=-V_{DC3}$ would produce the out-of-phase, “tuning fork” oscillation mode. For $V_{DC1}=-V_{DC2}$, and $V_{DC3}=0$ would produce the in-phase oscillation mode. These electrical excitations would produce electrostatic force on the oscillating masses from both the inner and outer electrostatic comb teeth capacitors. This configuration is also more robust in that all potentials are defined and none are left to float.

REFERENCES

- [1] Paula, Greg, "MEMS Sensors Branch Out," *Mechanical Engineering*, Oct. 1996, Vol. 118, No. 10, pp. 65-68.
- [2] Roszhart, T., "Micromachined Silicon Resonators," Conference Record IEEE Electro International, New York, NY, April 16-18, 1991, pp. 98-103.
- [3] Yun, W., and Howe, R. T., "Recent Developments in Silicon Microaccelerometers," *Sensors*, Oct. 1992, pp. 31-41.
- [4] Albert, W.C., "Monolithic Quartz Structure Vibrating Beam Accelerometer (VBA)," International Frequency Control Symposium, 1994, Boston, MA, June 1-3, 1994.
- [5] Zook, J.D., Burns, D.W., Guckel, H., Sniegowski, J.J., Engelstad, R.L., and Feng, A., "Resonant Microbeam Strain Transducers," *IEEE*, 1991, pp 529-532.
- [6] Blow, B.A., Harjani, R., Polla, D.L. and Tamagawa, T., "A Dual Frequency Range Integratrated Circuit Accelerometer Using Capacitive and Piezoelectric Sensing Techniques," IEEE International Symposium on Circuits and Systems, 1993, Vol. 2, pp 1120-1123.
- [7] Jones, R.E., "Micromachined Silicon Accelerometers for Inertial Sensing," IEEE Colloquium on Heading Sensors for Sonar Marine Applications (Digest No. 1994/004), Jan. 12, 1994, pp 8/1-4.
- [8] Barbour, N., Connelly, J., Gilmore, J., Greiff, P., Kourepenis, A. and Weinberg, M., "Micro-Electomechanical Istrument and Systems Development at Draper Laboratory," 3rd St. Petersburg International Conference on Integrated Navigation Systems, St.Petersburg, Russia, May 1996.
- [9] Burns, D.W., Horning, R.D., Herb, W.R., Zook, J.D., and Guckel, H., "Resonant Microbeam Accelerometers," *Euroensors & Transducers*, 1995, pp 659-661.
- [10] Weinberg, M., Bernstein, J., Cho, S., King, A.T., Kourepenis, A, Ward, P. and Sohn, J., "A Micromachined Comb Drive Tuning Fork Gyroscope for Commercial Applications," Sensors Expo, 2nd St. Petersburg International Conference on Gyroscopic Technology and Navigation, May 24-25, 1995.
- [11] Roark, R. J. and Young, W.C., "Beams; Flexure of Straight Bars," Formulas for Stress and Strain, Fifth Edition, McGraw-Hill, Inc., 1975.

- [12] Rao, S. S., Mechanical Vibrations, Second Edition, Addison-Wesley Publishing Co., 1990.
- [13] Derivation developed through personal conversation with Dr. Marc S. Weinberg, Draper Laboratory.
- [14] Carlson, B. A. and Gisser, D. G., Electrical Engineering: Concepts and Applications, Second Edition, Addison-Wesley Publishing Co., 1990.
- [15] Electrical analysis developed with Professor David L. Trumper, MIT.
- [16] Nayfeh, A. H. and Mook, D. T., Nonlinear Oscillations, John Wiley & Sons, Inc., New York, 1979.
- [17] Elwell, J. M., "Micromechanical Inertial Sensors for Commercial and Military Applications," Proceedings, 50th Annual Meeting of the Institute of Navigation, June 6-8, 1994, pp. 381-386.
- [18] Crandall, S. H., Dahl, N. C., editors, An Introduction to the Mechanics of Solids, McGraw Hill Book Co., New York, 1959.
- [19] Wortman, J. J. and Evans, R. A., "Young's Modulus, Shear Modulus, and Poisson's Ratio in Silicon and Germanium," *Journal of Applied Physics*, Vol. 36, No. 1, Jan. 1965.
- [20] Metzger H., and Kessler, F. R. , "The Debye-Sear Effect for the Determination of the Elastic Constants of Silicon," *Zeitschrift fur Naturforschung A (Astrophysik, Physik und Physikalische Chemie)*, Vol. 25, No. 6, pp 904-908.
- [21] McSkimmin, H. J., "Measurements of Elastic Constants at Low Temperatures by Means of Ultrasonic Waves," *Journal of Applied Physics*, Vol. 24, No. 8, Aug. 1953.
- [22] Cabuz, C., Fukatsu, K., Kurabayashi, T., Minami, K. and Esashi, M., "Microphysical Investigations on Mechanical Structures Realized in p+ Silicon," *Journal of Micromechanical Systems*, September 1995, Vol. 4, No. 3, pp 109-118.
- [23] Finite element analysis routines developed with Dr. David S. Nokes, Draper Laboratory.
- [24] ANSYS User's Manual, ANSYS Revision 5.2, Aug. 31, 1995.
- [25] Blevins, R.D., "Plates," Formulas for Natural Frequency and Mode Shape, Robert E. Krieger Publishing Co., Inc., 1979.
- [26] Probe test electrical excitation models developed with Anthony S. Kourepenis, Draper Laboratory.

LIST OF APPENDICES

	<u>Page</u>
Appendix A: Preliminary Design Spreadsheet	93
Appendix B: Corning #7740 Pyrex Material Information Sheet	96
Appendix C: Preliminary Design Spreadsheet Data	100

Appendix A: Preliminary Design Spreadsheet

Properties and Parameters					
Young's Mod. Si *	N/m ²	Em	1.65E+11		
density Si *	kg/m ³	rho	2.30E+03		
Permittivity of free space *	C ² /(N-m ²)	perm	8.85E-12		
Vibrating Beam parameters					
4 beams per proof mass					
base * (thickness)	m	bb	1.20E-05		
height * (beam width)	m	hb	4.00E-06		
Length * (Double length)	m	Lb	6.06E-04		
Moment of Inertia (Icx)	m ⁴	lb	6.40E-23		=bb*hb ³ /12
Oscillating Proof Mass Parameters					
thickness *	m	tpm	1.20E-05		=bb
width *	m	wpm	1.50E-04		
length *	m	Lpm	1.50E-04		
mass (4 per accelerometer)	kg	mpm	6.21E-10		=rho*tpm*wpm*Lpm
Calculate Force from acceleration					
acceleration	g	gacc	1.00E+00		
acceleration for gacc *	m/s ²	acc	9.81E+00		=9.81*gacc
side a for square *					
accelerometer mass	m	sideline	2.40E-03		
accelerometer mass for gacc	kg	ma	1.59E-07		=rho*(sideline) ² *tpm
	N	Fto	0.00		
Tensile Force for shift	N	Ft	1.56E-06		=ma*acc
Natural Frequency Calculations					
Stiffness of vib beams	N/m	kbo	18.22121		=((384*Em*Ib)/(Lb) ³)+(0.6*Fto/Lb))
Stiffness of vib beams under tension	N/m	kb	18.22276		=((384*Em*Ib)/(Lb) ³)+(0.6*Ft/Lb))
Nat. freq. of beams (no tension)	rad/sec	wno	1.71E+05		=SQRT(kbo/mpm)
	Hz	fno	2.7262E+04		=wno/(2*PI())

Natural Frequency under Tension Calculations				
Nat. freq. of beams under tension	rad/sec	wn	1.71E+05	=SQRT(kb/mpm)
	Hz	fn	2.7263E+04	=wn/(2*PI())
Shift in Nat. freq. (one-side)	rad/sec	dwn	7.26E+00	=wn-wno
	Hz	dfn	1.16	=dwn/(2*PI())
Scale Factor (two-sided)	Hz/g	SFline	2.31	=dfn/gacc*2
del f/f/g	1/g	SFline	8.47E-05	=SFline/fno
Comb Drive Calculation				
Drive element length *	microns	Lcdr	150.00	
Sense element length *	microns	Lcsn	150.00	
air gap *	microns	gapcdr	2.00	
length of drive tooth *	microns	ldrt	16.00	
overlap of teeth *	microns		8.00	
width of drive tooth *	microns	wcdr	4.00	
Number of active edges *		Ncdr	26.00	
Bias voltage *	V	Vbdr	2.00	
Drive amplitude *	V	Vadr	1.00	
Force Amplitude	N	Fcdr	2.76E-09	=Ncdr*perm*Vbdr*Vadr*tpm*10^6/gapcdr
Quality Factor *		Qcd	10000	
Displacement Amplitude at wn	m	Dispcdr	0.000002	=Qcd*Fcdr/kb
Capacitor Magnitude	F	Ccdr	1.10E-14	=(Ncdr*perm*tpm*ldrt/gapcdr)*0.5
Sense Capacitor per length	F/m	Ccsn	1.38E-09	=Ncdr*perm*tpm*10^6/gapcdr
Delta C	F	dCcsn	2.09E-15	=Ccsn*Dispcdr
Preamp Feedback Capacitance *	F	Cfb	2.00E-12	
Node Capacitance *	F	Co	4.00E-12	
Sense Bias Voltage *	V	Vbscn	5.00E+00	
Output Voltage Signal	V	Vocsn	0.0052	=dCcsn/(Cfb)*Vbscn

Appendix B: Corning #7740 Pyrex Material Information Sheet

Corning Code: 7740

Description

Glass Type --- Soda borosilicate

Color --- clear

Forms available --- pressed items, tubing, rolled sheet, blown ware, frit

Principal uses --- general

Properties

<u>Mechanical</u>	<u>Metric</u>	<u>English</u>
Density	2.23 g/cm ³	139.2 lb/ft ³
Young's Modulus	6.4 x 10 ³ kg/mm ²	9.1 x 10 ⁶ psi
Poisson's Ratio	0.20	
Shear Modulus	2.67 x 10 ³ kg/mm ²	3.8 x 10 ⁶ psi
Knoop Hardness (KHN ₁₀₀)	418	

<u>Viscosity</u>	<u>Metric</u>	<u>English</u>
Working Pt. (10 ⁴ poises)	1252°C	2286°F
Softening Pt. (10 ^{7.6} poises)	821°C	1510°F
Annealing Pt. (10 ¹³ poises)	560°C	1040°F
Strain Pt. (10 ¹⁴ poises)	510°C	950°F

<u>Thermal</u>	<u>Metric</u>	<u>English</u>
Coefficient of Expansion (0-300°C)	32.5 x 10 ⁻⁷ /°C	18.1 x 10 ⁻⁷ /°F
(25°C to Set Point 515°C)	35.0 x 10 ⁻⁷ /°C	19.5 x 10 ⁻⁷ /°F
Special Heat. 25°C	0.18 cal/g°C	0.18 Btu/lb°F
Thermal Conductivity. 25°C	0.0027 $\frac{\text{cal cm}}{\text{sec cm}^2 \text{ } ^\circ\text{C}}$	0.63 $\frac{\text{Btu ft}}{\text{h ft}^2 \text{ } ^\circ\text{F}}$
Thermal Diffusivity. 25°C	0.0069 cm ² /sec	0.00107 in ² /sec

Optical

Refractive Index (589.3 nm) 1.474

Birefringence Constant 394 $\frac{\text{nm}}{\text{cm}}$
kg/mm²Transmission @440nm 91.0%
560nm 90.8%

*Through a sample thickness 1.0 mm

ElectricalLog₁₀ Volume Resistivity @250°C 8.1 ohm-cm
@350°C 6.6 ohm-cm

Dielectric Constant @20°C: 1 MHz 4.6

Loss Tangent @20°C: 1 MHz 0.4%

Chemical

Weathering * 1

Acid Durability ** 1

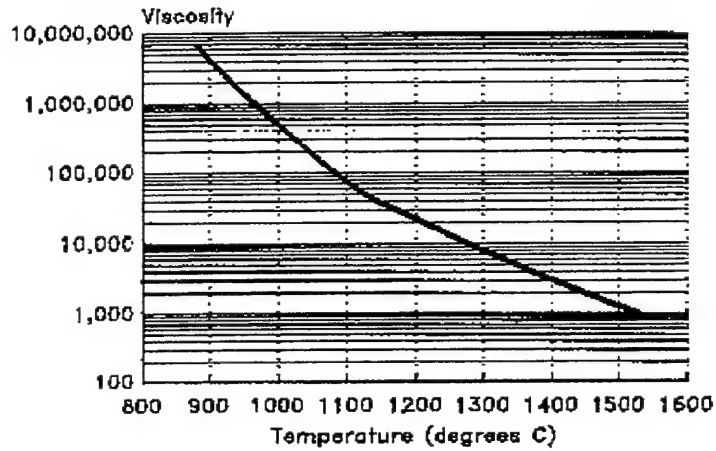
* Weathering is defined as corrosion by atmospheric-borne gases and vapors such as water and carbon dioxide. Glasses rated 1 will almost never show weathering effects; those rated 2 will occasionally be troublesome, particularly if weathering products cannot be removed; those glasses rated 3 require more careful consideration.

** The Acid Durability column classifies glasses according to their behavior in 5% hydrochloric acid at 95°C (203°F) for 24 hours.

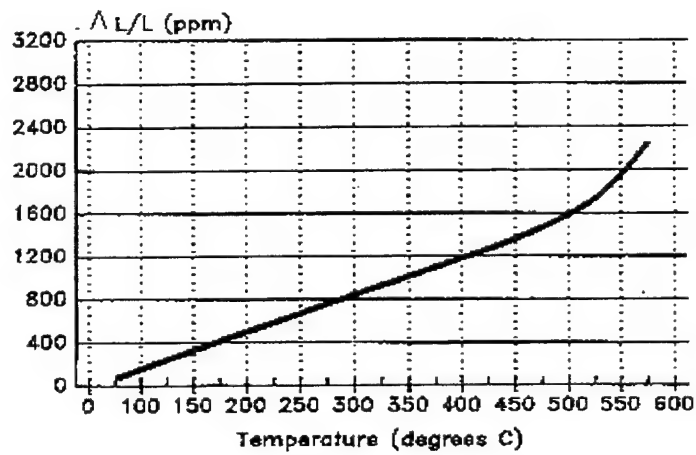
Classification	Thickness Loss (in.)
1	< 10 ⁻⁶
2	10 ⁻⁶ — 10 ⁻⁵
3	10 ⁻⁵ — 10 ⁻⁴
4	> 10 ⁻⁴

Values are listed with four degrees of accuracy. Those that are underscored (e.g. 2) result from recent determination and are reliable. Values not underscored are estimates offered with confidence. When two values are listed with one underscored, this indicates the range within which the true value lies: the underscored value is the more probable one (e.g. 2-3). A question mark indicates considerable uncertainty.

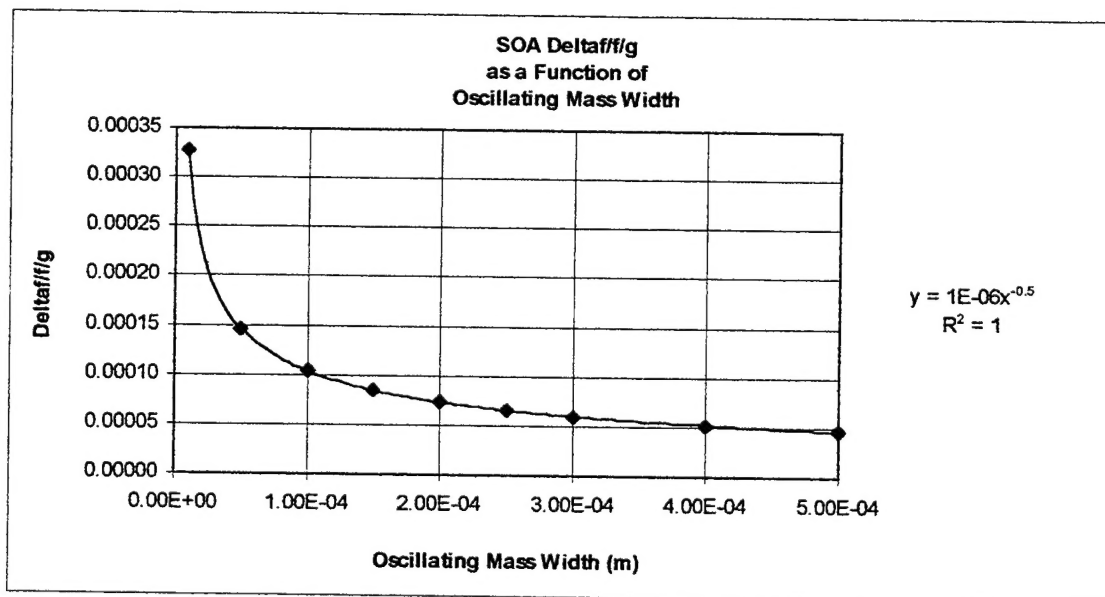
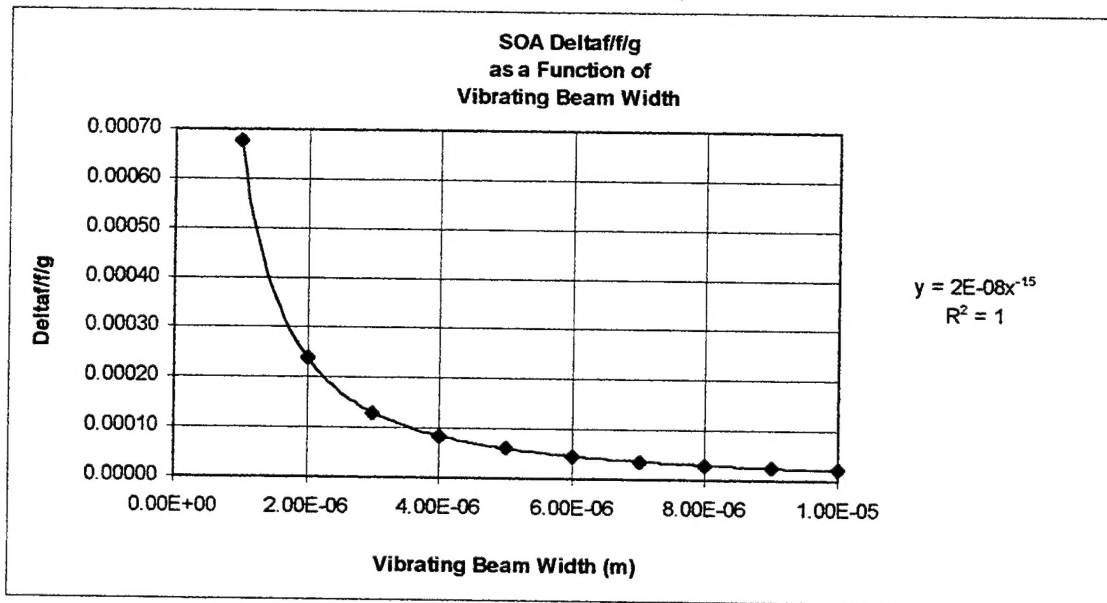
VISCOSITY

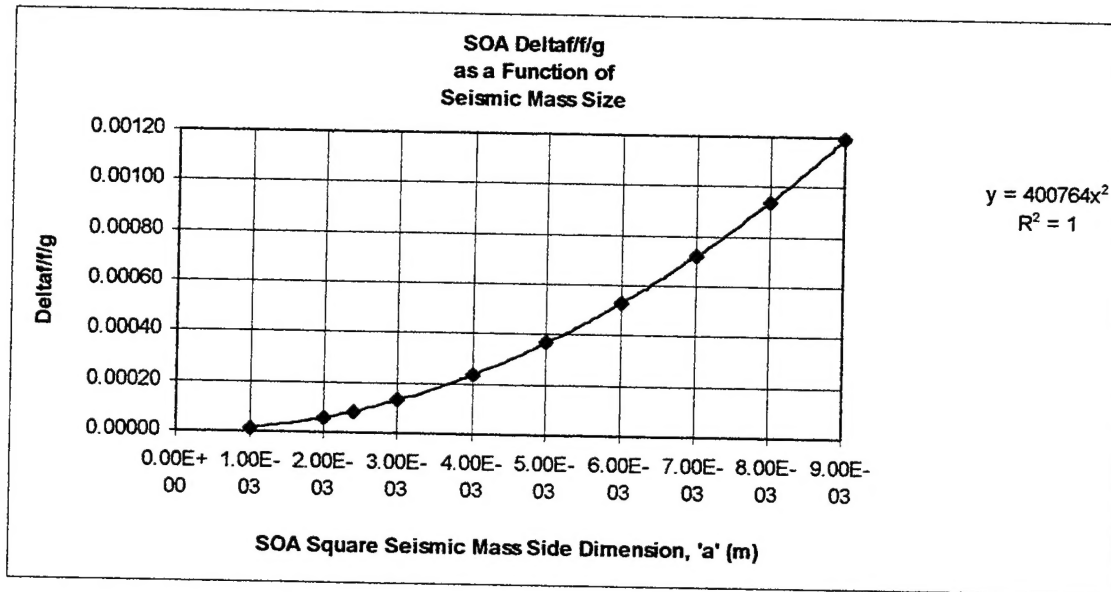


THERMAL EXPANSION



Appendix C: Preliminary Design Spreadsheet Data





REFERENCES

- [1] Paula, Greg, "MEMS Sensors Branch Out," *Mechanical Engineering*, Oct. 1996, Vol. 118, No. 10, pp. 65-68.
- [2] Roszhart, T., "Micromachined Silicon Resonators," Conference Record IEEE Electro International, New York, NY, April 16-18, 1991, pp. 98-103.
- [3] Yun, W., and Howe, R. T., "Recent Developments in Silicon Microaccelerometers," *Sensors*, Oct. 1992, pp. 31-41.
- [4] Albert, W.C., "Monolithic Quartz Structure Vibrating Beam Accelerometer (VBA)," International Frequency Control Symposium, 1994, Boston, MA, June 1-3, 1994.
- [5] Zook, J.D., Burns, D.W., Guckel, H., Sniegowski, J.J., Engelstad, R.L., and Feng, A., "Resonant Microbeam Strain Transducers," *IEEE*, 1991, pp 529-532.
- [6] Blow, B.A., Harjani, R., Polla, D.L. and Tamagawa, T., "A Dual Frequency Range Integratrated Circuit Accelerometer Using Capacitive and Piezoelectric Sensing Techniques," IEEE International Symposium on Circuits and Systems, 1993, Vol. 2, pp 1120-1123.
- [7] Jones, R.E., "Micromachined Silicon Accelerometers for Inertial Sensing," IEEE Colloquium on Heading Sensors for Sonar Marine Applications (Digest No. 1994/004), Jan. 12, 1994, pp 8/1-4.
- [8] Barbour, N., Connelly, J., Gilmore, J., Greiff, P., Kourepenis, A. and Weinberg, M., "Micro-Electomechanical Istrument and Systems Development at Draper Laboratory," 3rd St. Petersburg International Conference on Integrated Navigation Systems, St.Petersburg, Russia, May 1996.
- [9] Burns, D.W., Horning, R.D., Herb, W.R., Zook, J.D., and Guckel, H., "Resonant Microbeam Accelerometers," *Eurosensors & Transducers*, 1995, pp 659-661.
- [10] Weinberg, M., Bernstein, J., Cho, S., King, A.T., Kourepenis, A., Ward, P. and Sohn, J., "A Micromachined Comb Drive Tuning Fork Gyroscope for Commercial Applications," Sensors Expo, 2nd St. Petersburg International Conference on Gyroscopic Technology and Navigation, May 24-25, 1995.
- [11] Roark, R. J. and Young, W.C., "Beams; Flexure of Straight Bars," *Formulas for Stress and Strain*, Fifth Edition, McGraw-Hill, Inc., 1975.

- [12] Rao, S. S., Mechanical Vibrations, Second Edition, Addison-Wesley Publishing Co., 1990.
- [13] Derivation developed through personal conversation with Dr. Marc S. Weinberg, Draper Laboratory.
- [14] Carlson, B. A. and Gisser, D. G., Electrical Engineering: Concepts and Applications, Second Edition, Addison-Wesley Publishing Co., 1990.
- [15] Electrical analysis developed with Professor David L. Trumper, MIT.
- [16] Nayfeh, A. H. and Mook, D. T., Nonlinear Oscillations, John Wiley & Sons, Inc., New York, 1979.
- [17] Elwell, J. M., "Micromechanical Inertial Sensors for Commercial and Military Applications," Proceedings, 50th Annual Meeting of the Institute of Navigation, June 6-8, 1994, pp. 381-386.
- [18] Crandall, S. H., Dahl, N. C., editors, An Introduction to the Mechanics of Solids, McGraw Hill Book Co., New York, 1959.
- [19] Wortman, J. J. and Evans, R. A., "Young's Modulus, Shear Modulus, and Poisson's Ratio in Silicon and Germanium," *Journal of Applied Physics*, Vol. 36, No. 1, Jan. 1965.
- [20] Metzger H., and Kessler, F. R. , "The Debye-Sear Effect for the Determination of the Elastic Constants of Silicon," *Zeitschrift fur Naturforschung A (Astrophysik, Physik und Physikalische Chemie)*, Vol. 25, No. 6, pp 904-908.
- [21] McSkimmin, H. J., "Measurements of Elastic Constants at Low Temperatures by Means of Ultrasonic Waves," *Journal of Applied Physics*, Vol. 24, No. 8, Aug. 1953.
- [22] Cabuz, C., Fukatsu, K., Kurabayashi, T., Minami, K. and Esashi, M., "Microphysical Investigations on Mechanical Structures Realized in p+ Silicon," *Journal of Micromechanical Systems*, September 1995, Vol. 4, No. 3, pp 109-118.
- [23] Finite element analysis routines developed with Dr. David S. Nokes, Draper Laboratory.
- [24] ANSYS User's Manual, ANSYS Revision 5.2, Aug. 31, 1995.
- [25] Blevins, R.D., "Plates," Formulas for Natural Frequency and Mode Shape, Robert E. Krieger Publishing Co., Inc., 1979.
- [26] Probe test electrical excitation models developed with Anthony S. Kourepenis, Draper Laboratory.